Applications of diffusion MRI: Tensor-valued encoding, time-dependent diffusion, and histological validation

Brabec, Jan

2022

Document Version:
Publisher's PDF, also known as Version of record

Applications of diffusion MRI:
Tensor-valued encoding, time-dependent diffusion, and histological validation

JAN BRABEC
MEDICAL RADIATION PHYSICS | FACULTY OF SCIENCE | LUND UNIVERSITY

Applications of diffusion MRI

Applications of diffusion MRI

Tensor-valued encoding, time-dependent diffusion, and histological validation

Jan Brabec

LUND
UNIVERSITY

DOCTORAL DISSERTATION

Doctoral dissertation for the degree of Doctor of Philosophy (PhD) at the Faculty of Science at Lund University to be publicly defended on Friday, 7th of October at 9 a.m. in Lundmarksalen, Astronomihuset, Sölvegatan 27, Lund, Sweden.

Faculty opponent
Prof. Mark Does, Department of Biomedical Engineering, Vanderbilt University, 5824 Stevenson Center, Nashville, TN 37232, USA.

Organization	Document name
LUND UNIVERSITY Faculty of Sciences Clinical Sciences Lund Department of Medical Radiation Physics	DOCTORAL DISSERTATION
	Date of disputation: 7th October 2022
Author(s): Jan Brabec	Sponsoring organization

Title and subtitle: Applications of diffusion MRI: Tensor-valued encoding, time-dependent diffusion, and histological validation

Abstract:

Diffusion MRI (dMRI) sensitizes the MR signal to the diffusion of water molecules at the microscopic level and thereby non-invasively probes tissue microstructure. This is relevant when determining biological properties of tissues, for example, cancer type and its malignancy. The problem is, however, that dMRI lacks sensitivity and specificity to distinct microstructural features because an image voxel contains vast number of different features that are mapped onto relatively few dMRI observables. To tackle this issue, we aimed at solving two gaps in current knowledge—the first was related to what microstructural aspects are of most importance and the second to how adding new observables to the dMRI measurement could improve brain tumor imaging.

In this work, we first investigate the biological underpinnings of dMRI observables—focusing on the degree to which larger-scale microstructural arrangements are of relevance. In Paper I, we investigated the effects of non-straight propagation of axons and found that they are indistinguishable from those originating from the diameter of a straight axon, at least for typical measurements with a clinical scanner. We propose that the use of short diffusion times could help separate them. In Paper II, in a comparison between histology and microimaging of meningioma brain tumors, we quantified to what degree the common biological interpretation of one of the most used dMRI observable holds—mean diffusivity (MD) as reflecting cell density and fractional anisotropy reflecting tissue anisotropy. We found that the local variability in MD was explained in minority of the samples whereas FA in majority by the common interpretations. We suggested additional relevant features such as tumor vascularization, psammoma bodies, microcysts or tissue cohesivity for explaining MD variability.

Second, we examined whether a framework that introduces a new measurement observable brings value in intracranial tumor imaging. This new variable is termed the b-tensor shape and is derived from the tensor-valued dMRI paradigm. In Paper IV, we adjusted and shortened by 40 % (from 5 to 3 minutes) a tensor-valued dMRI protocol for clinical imaging of intracranial tumors and applied it to characterize to a wide range of different intracranial tumors. The protocol was also used in clinical studies of patients with intracranial tumors—gliomas and meningiomas—in Paper III and Paper V, respectively. In Paper III, we found that using so-called spherical b-tensor encoding leads to enhanced conspicuity of glioma hyperintensities to white matter in all patients and on average the signal-intensity-ratio increased by 28 %. In Paper V we found that it may also inform on meningiomas preoperatively. The standard deviation of isotropic kurtosis was associated with tumor grade and with and the 10th percentiles of the mean and anisotropic kurtoses with firm tumor consistency. Preoperative knowledge of the consistency is important for the neurosurgeons when choosing the optimal surgical procedure.

Key words

Classification system and/or index terms (if any)

Supplementary bibliographical information		**Language: English**
ISSN and key title		**ISBN** 978-91-8039-343-0 (electronic) 978-91-8039-344-7 (print**)**
Recipient's notes	**Number of pages:** 91	Price
	Security classification	

Signature 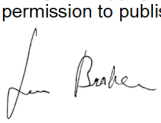 Date 2022-08-18

Applications of diffusion MRI

Tensor-valued encoding, time-dependent diffusion, and histological validation

Jan Brabec

LUND
UNIVERSITY

Faculty of Science
Department of Medical Radiation Physics

978-91-8039-343-0 (electronic)
978-91-8039-344-7 (print)

Printed in Sweden by Media-Tryck, Lund University
Lund 2022

To my grandfather for his contributions to NMR.

Table of Contents

Abstract

Diffusion MRI (dMRI) sensitizes the MR signal to the diffusion of water molecules at the microscopic level and thereby non-invasively probes tissue microstructure. This is relevant when determining biological properties of tissues, for example, cancer type and its malignancy. The problem is, however, that dMRI lacks sensitivity and specificity to distinct microstructural features because an image voxel contains vast number of different features that are mapped onto relatively few dMRI observables. To tackle this issue, we aimed at solving two gaps in current knowledge—the first was related to what microstructural aspects are of most importance and the second to how adding new observables to the dMRI measurement could improve brain tumor imaging.

In this work, we first investigate the biological underpinnings of dMRI observables—focusing on the degree to which larger-scale microstructural arrangements are of relevance. In Paper I, we investigated the effects of non-straight propagation of axons and found that they are indistinguishable from those originating from the diameter of a straight axon, at least for typical measurements with a clinical scanner. We propose that the use of short diffusion times could help separate them. In Paper II, in a comparison between histology and microimaging of meningioma brain tumors, we quantified to what degree the common biological interpretation of one of the most used dMRI observable holds—mean diffusivity (MD) as reflecting cell density and fractional anisotropy reflecting tissue anisotropy. We found that the local variability in MD was explained in minority of the samples whereas FA in majority by the common interpretations. We suggested additional relevant features such as tumor vascularization, psammoma bodies, microcysts or tissue cohesivity for explaining MD variability.

Second, we examined whether a framework that introduces a new measurement observable brings value in intracranial tumor imaging. This new variable is termed the b-tensor shape and is derived from the tensor-valued dMRI paradigm. In Paper IV, we adjusted and shortened by 40 % (from 5 to 3 minutes) a tensor-valued dMRI protocol for clinical imaging of intracranial tumors and applied it to characterize to a wide range of different intracranial tumors. The protocol was also used in clinical studies of patients with intracranial tumors—gliomas and meningiomas—in Paper III and Paper V, respectively. In Paper III, we found that using so-called spherical b-tensor encoding leads to enhanced conspicuity of glioma hyperintensities to white matter in all patients and on average the signal-intensity-ratio increased by 28 %. In Paper V we found that it may also inform on meningiomas preoperatively. The standard deviation of isotropic kurtosis was associated with tumor grade and with and the 10^{th} percentiles of the mean and anisotropic kurtoses with firm tumor consistency. Preoperative knowledge of the consistency is important for the neurosurgeons when choosing the optimal surgical procedure.

Populärvetenskaplig sammanfattning

Cancer är en stor orsak till dödsfall i den industrialiserade världen. För att diagnosticera hjärntumörer och utvärdera effektivitet av terapi så spelar medicinsk bildtagning en stor roll. Diffusionsviktad magnetresonanstomografi (dMRT) är en bildtagningsteknik som ger information om vävnadens mikrostruktur. Denna information är av stor betydelse för både diagnostik och terapi. Det är idag dock inte helt uppenbart exakt vilka aspekter i vävnadens mikrostruktur som är har störst inflytande på bilder tagna med dMRT. Vävnad innehåller ett stort antal olika cellulära strukturer av olika form och storlek och dMRI ger bara information om deras genomsnitt. Målet med denna avhandling är att undersöka och överbrygga två kunskapsbrister i dMRT – den första relaterar till vilka vävnadsstrukturer som är av störst betydelse för dMRT bilder och den andra relaterar till huruvida en ny slags dMRI-mätning kan leda till förbättrad bildtagning av hjärntumörer.

För att uppnå det första målet så undersöktes sambandet mellan egenskaper i vävnad och resultat från dMRT. Genom att analysera en modell av axoner i hjärnans vita vävnad påvisades att egenskaper hos geometrin av axonens bana inte kan särskiljas från dess diameter vid vanliga dMRT mätningar (Paper I). För att separera dem behövs variation av tiden under vilken diffusion observeras (den s.k. diffusionstiden), och då framför allt kortare tider. Utöver axoner undersöktes även meningiom, som är en slags tumör som utgår från hjärnhinnan. Genom att jämföra dMRT bilder och mikroskopibilder av samma tumör påvisades att inte bara celltäthet påverkar dMRT, utan även andra vävnadsstrukturer som till exempel ansamling av kalcium (Paper II).

För att uppnå det andra målet undersöktes om en ny mätegenskap – formen på den så kallade ”b-tensorn”– kan förbättra resultaten vid undersökning av hjärntumörer. En inledande studien syftade till att förkorta undersökningstiden för dMRT med den nya metoden och karakterisera ett stort antal olika sorters hjärntumörer (Paper IV). Undersökningstiden var bara 3 minuter och metoden användes för att studera patienter med hjärntumörer – s.k. gliom (Paper III) och meningiom (Paper V). Den nya metoden visade sig ge förbättrad bildkontrast mellan gliom och vit hjärnsubstans hos alla patienter (Paper III). Metoden kan även vara till pre-operativ nytta hos patienter med meningiom, eftersom den kan ge bättre kunskap om tumörens egenskaper (Paper V). Exempelvis var tumörkonsistens och malignitet associerade med ny mätegenskap. Kännedom om dessa egenskaper kan vara till hjälp vid val av kirurgiskt ingrepp. Sammanfattningsvis ger den nya metoden information som inte kan erhållas med vanliga dMRT mätningar.

Original papers

This thesis is based on four publications and one manuscript, which are referred to by Roman numerals.

I. **Brabec J**, Lasič S, Nilsson M. Time-dependent diffusion in undulating thin fibers: Impact on axon diameter estimation. *NMR in Biomedicine* 2020 Mar;33(3):e4187. doi: 10.1002/nbm.4187.

II. **Brabec J**, Friedjungová M, Vašata D, Englund E, Bengzon J, Knutsson L, Szczepankiewicz F, Maly Sundgren P, Nilsson M. Mean diffusivity and fractional anisotropy at the mesoscopic level in meningioma tumors: Relation with cellularity and tissue anisotropy. *Manuscript*.

III. **Brabec J**, Durmo F, Szczepankiewicz F, Brynolfsson P, Lampinen B, Rydelius A, Knutsson L, Westin C-F, Maly Sundgren P, Nilsson M. Separating glioma hyperintensities from white matter by diffusion-weighted imaging with spherical tensor encoding. *Frontiers in Neuroscience* 2022 Apr 21;16:842242. doi: 10.3389/fnins.2022.842242.

IV. Nilsson M, Szczepankiewicz F, **Brabec J,** Taylor M, Westin C-F, Golby A, Westen D, Maly Sundgren P. Tensor-valued diffusion MRI in under 3 minutes: an initial survey of microscopic anisotropy and tissue heterogeneity in intracranial tumors. *Magnetic Resonance in Medicine 2020* Feb;83(2):608-620. doi: 10.1002/mrm.27959.

V. **Brabec J**, Szczepankiewicz F, Lennartsson F, Englund E, Pebdani H, Bengzon J, Knutsson L, Westin C-F, Maly Sundgren P, Nilsson M. Histogram analysis of tensor-valued diffusion MRI in meningiomas: Relation to consistency, histological grade and type. *NeuroImage: Clinical* 2022;33:102912. doi: 10.1016/j.nicl.2021.102912.

List of contributions

Below is a summary of my contributions to each published paper:

I. I participated in the study design, performed the data analysis and wrote the analysis code. In particular, I implemented analytical predictions and numerical simulations of the diffusion spectra, as well as the signal analysis. I was the main author of the paper.

II. I was responsible for the design of the study, data collection as well as data and statistical analysis. I also wrote the analysis code. In particular, I performed the co-registration and post-processing of histology and MR images and coordinated the collaboration with another research group that performed the deep learning analysis. I was the main author of the paper.

III. I was responsible for the study design, interpretation, data and statistical analysis and wrote the analysis code. Specifically, I proposed the use of the signal-intensity ratio as a key quantity and performed the image post-processing. I was the main author of the paper.

IV. I participated in the study design. I reviewed and contributed to the writing of the paper. I was the third author of the paper.

V. I was responsible for the study design, data and statistical analysis and wrote the analysis code. I proposed using the histogram analysis and conceived the use of rim regions-of-interest, as well as performed image post-processing. I was the main author of the paper.

Publications not included in the thesis

- Massion PP, Antic S, Ather S, Arteta C, **Brabec J**, Chen H, Declerck J, Dufek D, Hickes W, Kadir T, Kunst J. Assessing the accuracy of a deep learning method to risk stratify indeterminate pulmonary nodules. *American journal of respiratory and critical care medicine* 2020 Jul 15;202(2):241-9. doi: 10.1164/rccm.201903-0505OC.
- Chakwizira A, Westin CF, **Brabec J**, Lasič S, Knutsson L, Szczepankiewicz F, Nilsson M. Probing restricted diffusion and exchange using free gradient waveforms: validation by numerical simulations. *Under review in NMR in Biomedicine 2022*.
- **Brabec J**, Lennartsson F. Editorial for" Investigation of the Inter-and Intra-Scanner Reproducibility and Repeatability of Radiomics Features in Magnetic Resonance Imaging". *Journal of Magnetic Resonance Imaging: JMRI* 2022 Apr 1-2. doi: 10.1002/jmri.28190.

Conference abstracts

1. **Brabec J**, Lasič S, Nilsson M. Diffusion in Undulating Axons: Implications for Axon Diameter Mapping and its Potential Remedy. Oral presentation at ESMRMB 34th Annual Meeting, Barcelona, Spain, 2017.
2. **Brabec J**, Lasič S, Nilsson M. Simulation of diffusion in axons with harmonic and stochastic trajectories. Power pitch at ISMRM 26th Annual Meeting, Paris, France, 2018.
3. **Brabec J**, Szczepankiewicz F, Westin C-F, Golby A, van Westen D, Sundgren P-C, Nilsson M. B-tensor encoding is clinically feasible and may add relevant information in the work-up of patients with brain tumors. Oral presentation at Medicinteknikdagarna Annual Meeting, Umeå, Sweden, 2018.
4. **Brabec J**, Szczepankiewicz F, Englund E, Bengzon J, Knutsson L, Westin C-F, Sundgren P-C, Nilsson M. B-tensor encoding in meningiomas: Comparisons with histology, microimaging and tumor consistency. Oral presentation with summa cum laude award at ISMRM 27th Annual Meeting, Montreal, Canada, 2019.
5. **Brabec J**, Durmo F, Szczepankiewicz F, Lampinen B, Knutsson L, Sundgren P-C, Nilsson M. Classification of non-enhancing glioma tumors by diffusion MRI with B-tensor encoding. Oral presentation at ECR Annual Meeting, virtual, 2020.
6. Nilsson M, Westin C-F, **Brabec J**, Lasic S, Szczepankiewicz F. A unified framework for analysis of time-dependent diffusion: numerical validation of a restriction-exchange correlation experiment. Oral presentation at ISMRM 28th Annual Meeting, virtual, 2020.
7. Szczepankiewicz F, Juvekar P, **Brabec J**, Sundgren P-C, Nilsson M, Golby A, Westin C-F. Investigation of tumor grade and gadolinium enhancement by tensor-valued diffusion encoding and QTI analysis: an exploratory study of gliomas. Digital poster at ISMRM 28th Annual Meeting, virtual, 2020.
8. **Brabec J**, Szczepankiewicz F, Englund E, Bengzon J, Knutsson L, Westin C-F, Sundgren P-C, Nilsson M. Imaging meningioma tumor microstructure: a comparison between quantitative histopathology and high-resolution diffusion tensor imaging. Digital poster at ISMRM 28th Annual Meeting, virtual, 2020.
9. **Brabec J**, Durmo F, Szczepankiewicz F, Lampinen B, Knutsson L, Sundgren P-C, Nilsson M. B-tensor encoding in gliomas: improved tumor grading by the isotropic kurtosis. Oral presentation with summa cum laude

award and highlighted in diffusion highlights at ISMRM 28th Annual Meeting, virtual, 2020.

10. **Brabec J**, Durmo F, Szczepankiewicz F, Brynolfsson P, Lampinen B, Ondkova N, Knutsson L, Sundgren P-C, Nilsson M. Diffusion MRI with spherical B-tensor encoding increases glioma tumor conspicuity. Oral presentation in a featured content section at RSNA 106th Annual Meeting, virtual, 2020.
11. **Brabec J**, Szczepankiewicz F, Sramek J, Englund E, Bengzon J, Knutsson L, Westin C-F, Sundgren P-C, Nilsson M. Beyond cellularity: Which microstructural features determine the mesoscopic mean diffusivity in meningiomas? Digital poster at ISMRM 29th Annual Meeting, virtual, 2021.
12. **Brabec J**, Friedjungová M, Vašata D, Englund E, Knutsson L, Szczepankiewicz F, Sundgren P-C, Nilsson M. Explaining variation in DTI parameters with meningioma microscopy: A comparison between a neural network and an image-feature-based approach. Digital poster at ISMRM 30th Annual Meeting, London, United Kingdom, 2022.
13. **Brabec J**, Friedjungová M, Vašata D, Englund E, Knutsson L, Szczepankiewicz F, Sundgren P-C, Nilsson M. Mean diffusivity and fractional anisotropy at the mesoscopic level in meningioma tumors: Relation with cell density and tissue anisotropy. Oral presentation at ESNR 45th Annual Meeting, Lisbon, Portugal, 2022.

Abbreviations

ADC	Apparent diffusion coefficient
ANN	Artificial neural network
AUC	Area under curve
CD	Cell density
DDE	Double diffusion encoding
DKI	Diffusion kurtosis imaging
dMRI	Diffusion magnetic resonance imaging
DTD	Diffusion tensor distribution
DTI	Diffusion tensor imaging
DWI	Diffusion-weighted imaging
EPI	Echo-planar imaging
FA	Fractional anisotropy
FA_{IP}	In-plane fractional anisotropy
Gd	Gadolinium
H&E	Hematoxylin-eosin
IA	Image anisotropy
LTE	Linear b-tensor encoding
LTE-DWI	DWI obtained with linear b-tensor encoding
MD	Mean diffusivity
MK	Mean kurtosis
MK_A	Anisotropic kurtosis
MK_E	Effective kurtosis
MK_I	Isotropic kurtosis
MK_T	Total kurtosis
MR	Magnetic resonance
MRI	Magnetic resonance imaging
MSD	Mean squared displacement
NAWM	Normally appearing white matter
PAS	Principal axis system
PTE	Planar b-tensor encoding
QTI	Q-space trajectory imaging
R^2	Coefficient of determination
RF	Radio-frequency
ROI	Region of interest
SIR	Signal intensity ratio

STE	Spherical b-tensor encoding
STE-DWI	DWI obtained with spherical b-tensor encoding
T1w	T1-weighted
TDE	Triple diffusion encoding
TE	Echo time
V_A	Anisotropic variance
V_I	Isotropic variance
WHO	World health organization
WM	White matter
µFA	Microscopic fractional anisotropy

Mathematical symbols

Δ	Time between the onsets of diffusion gradients
$\langle \Delta x^2 \rangle$	Mean squared displacement
$\mathbf{B}$	B-tensor
b	Diffusion encoding strength, b-value
b_Δ	B-tensor shape
$\mathbb{C}$	Covariance tensor
$\mathbb{C}_I$	Isotropic covariance tensor
$\mathbf{D}$	Diffusion tensor
$\langle \mathbf{D} \rangle$	Voxel-averaged diffusion tensor
$\langle \mathbf{D} \rangle_I$	Isotropic voxel-averaged diffusion tensor
D	Diffusion coefficient
$D(f)$	Diffusion spectrum
D_0	Bulk diffusion coefficient
D_I	Isotropic diffusivity
$\mathbf{e}$	Vector containing experimental variables
exp	Exponential function
$\mathbf{g}$	Diffusion encoding gradient
G	Diffusion gradient strength
λ	Tortuosity coefficient
λ_i	I-th eigenvalue
$\mathbf{p}$	Vector containing model parameters
$\hat{\mathbf{p}}$	Vector containing estimated model parameters
$\mathbf{R}$	Rotation matrix
$\mathbf{r}$	Spin position in 3-dimensional space
S	Diffusion signal
S_0	Signal without diffusion encoding
$\bar{S}$	Powder-averaged diffusion signal
t	Time
t_0	Starting time
t_D	Diffusion time
t_{eff}	Effective diffusion time

$\mathbf{u}$	Encoding direction in 2- or 3-dimensional space
x	Spin position or encoding direction along x direction
γ	Gyromagnetic ratio
δ	Duration of a single pulsed diffusion encoding
Φ	Phase acquired by diffusion encoding
J_ν	ν-nth order Bessel function
$\mathcal{F}$	Fourier transformation
$\lvert q(f)\rvert^2$	Encoding power spectrum

Mathematical operators

$\langle\cdot\rangle$	Average
$[\cdot] : [\cdot]$	Double inner product
$[\cdot]\otimes[\cdot]$	Outer product
$E_\lambda[\cdot]$	Average across tensor eigenvalues
$V_\lambda[\cdot]$	Variance across tensor eigenvalues

1. Introduction

Diffusion MRI (dMRI) non-invasively probes tissue microstructure, i.e. the arrangements of cell structures on the micrometer length-scale (Le Bihan, 2003). Knowledge of the tissue microstructure is important for medical care, as the microstructure is related to important biological properties such as tumor type or malignancy. Diffusion MRI is sensitive to microstructure because microscopic structures hinder the random motion of water molecules that results from the molecular thermal energy and thereby leave a mark on the diffusion process (called Brownian or self-diffusion) (Einstein, 1905). In practice, the signal from magnetic resonance imaging (MRI) can be sensitized to the diffusion of water by the use of diffusion-encoding gradients (Stejskal and Tanner, 1965;Brown et al., 2014). This allows diffusion and thus microstructure to be indirectly and non-invasively probed.

Diffusion MRI has been widely used clinically because it has shown benefits for patients in settings such as stroke care, cancer care and neurosurgery planning. In stroke, this is because the apparent diffusion coefficient (ADC) obtained from diffusion-weighted imaging (DWI) is sensitive to ischemia (Moseley et al., 1990). Interestingly, the biophysical underpinnings remain elusive (Blackband et al., 2020). In cancer imaging, DWI and ADC maps are regularly inspected in patients with intracranial tumors. This is because ADC was shown to be inversely proportional to cell density (Chen et al., 2013) and thereby indicates viable tumor regions. Furthermore, presence of high-signal values on DWI scans, referred to as DWI-hyperintensities, is associated with worse prognosis (Kolakshyapati et al., 2017;Zeng et al., 2018;White et al., 2019). Fractional anisotropy (FA) from diffusion tensor imaging (DTI) can identify displaced white matter tracts by a tumor and assess their disruption and tumor infiltration (Price et al., 2004;Jütten et al., 2019) and may provide insight preoperatively concerning whether they are salvageable (Yen et al., 2009). Mean kurtosis (MK) from diffusion kurtosis imaging (DKI) can improve tumor classification and monitoring (Kang et al., 2011;Van Cauter et al., 2012;Vandendries et al., 2014;Delgado et al., 2017). Moreover, diffusion MRI is sensitive to the anisotropic diffusion in axons (Beaulieu, 2002) and by connecting the predominant direction of the diffusion it can be used to non-invasively visualize major nerve tracts, which is referred to as tractography (Mori et al., 1999). Such methods are important in neurosurgical planning to avoid regions of healthy white matter during neurosurgery (Bulakbasi, 2009;Romano et al., 2009;Essayed et al., 2017).

However, it is not clear which microstructural features are imprinted in a dMRI signal, and, moreover, at the typical image resolution each image voxel will contain multiple microenvironments, but these are mapped onto only relatively few dMRI observables (Nilsson et al., 2018;Novikov et al., 2018;Alexander et al., 2019). For example, the signal can be measured with respect to the diffusion encoding strength, i.e. the *b*-value, and the diffusion signal vs *b*-value for moderate *b*-values yields just two observables—its initial slope and its departure from exponential decay at higher *b*-values. The first observable is the one obtained with DWI and the second with DKI. The measurements can be performed in several directions, which adds the voxel-level anisotropy (difference in diffusion between directions) as another observable in DTI (Basser et al., 1994).

Microstructure modelling has been proposed as a means to move from mapping unspecific observables such as ADC, FA, and MK to mapping specific microstructure quantities such as cell density in cancers or axon diameters in white matter. In such microstructure models, the tissue geometry is represented by a biophysical model and, in principle, two problems need to be solved: the forward problem that predicts the diffusion signal for given model parameters and a certain diffusion encoding protocol, and the inverse problem that estimates the model parameters from the measured signal. In the construction of the forward problem, it is not always clear which features are of most relevance (Novikov et al., 2018). When solving the inverse problem, one may find that the diffusion encoding protocol may not be sensitive to all microstructural features incorporated in the model, which means that many solutions may fit the observed data equally well (Jelescu et al., 2016;Lampinen et al., 2020a). To illustrate the problem, consider white matter microstructure modelling. Early models represented the axons in white matter as prolate ellipsoids (Stanisz et al., 1997) or straight impermeable cylinders (Assaf and Basser, 2005;Assaf et al., 2008;Alexander et al., 2010). Such models provided axon diameter estimates, but these were higher than expected from histology (Assaf et al., 2008;Barazany et al., 2009;Alexander et al., 2010). Although those early models were appealing in their simplicity, they were incomplete descriptions that provided biased estimates. Importantly, these early modelling attempts did not incorporate broader features of the whole biological system, such as the non-straight axon propagation known as undulations, which were later shown to have a strong impact on the dMRI signal (Paper I)(Nilsson et al., 2012;Lee et al., 2020a;Lee et al., 2020b). Another feature is the variation of the axon diameter along its path (Abdollahzadeh et al., 2019;Lee et al., 2020b). Fine microstructural details such as axonal spines, leaflets, or beads could also be important to consider (Palombo et al., 2018;Lee et al., 2020b). This highlights that progression in dMRI demands a deeper understanding of which features of the microstructure are encoded into the signal.

The microstructure modelling work has also highlighted that the majority of dMRI experiments use methods that yield too few observables to infer specific information on the microstructure (Lampinen et al., 2017;de Almeida Martins and Topgaard, 2018;Novikov et al., 2019;Jelescu et al., 2020;Slator et al., 2021). This is because contemporary applications rely on diffusion encoding by a pair of pulsed gradients (Stejskal and Tanner, 1965), developed in the 1960s. New dMRI observables can be added by implementing new approaches of performing diffusion encoding. A natural step forward is to extend the measurement by one or two pairs of gradients, which is referred to as double or triple diffusion encoding (DDE or TDE) (Shemesh et al., 2016). These and other diffusion encoding strategies can be generalized into so-called tensor-valued dMRI (Westin et al., 2016). This framework generalizes the concept of a *b*-value into a b-tensor that allows for a new measurement variable—the b-tensor shape (Eriksson et al., 2013;Lasič et al., 2020). So-called b-tensor encoding is typically executed not by pulsed gradients but by free gradient waveforms (Szczepankiewicz et al., 2021b). These can be optimized to minimize echo time (Sjölund et al., 2015), concomitant gradient effects (Szczepankiewicz et al., 2019b), cross-terms with background gradients (Szczepankiewicz and Sjölund, 2021), motion (Szczepankiewicz et al., 2021a;Lasič et al., 2022) or designed to exploit time-dependent diffusion (Lundell et al., 2019;Chakwizira et al., 2021). Tensor-valued encoding can also be used in models to disentangle the MK from DKI into two components—anisotropic and isotropic kurtoses (MK_A and MK_I, respectively)—where MK is its sum. This is beneficial because MK_A is related to microscopic tissue anisotropy, whereas MK_I is related to cell density variance, which are two orthogonal microstructural features (Szczepankiewicz et al., 2016). We will refer to tensor-valued dMRI performed to obtain MK_A and MK_I as Q-space Trajectory Imaging (QTI) (Szczepankiewicz et al., 2016;Westin et al., 2016). Tensor-valued dMRI has so far demonstrated utility in conditions such as the modelling of brain microstructure (Szczepankiewicz et al., 2015;Lampinen et al., 2017;Dhital et al., 2018;Lampinen et al., 2019;Szczepankiewicz et al., 2019a;Afzali et al., 2020;Lampinen et al., 2020a;Afzali et al., 2021;de Almeida Martins et al., 2021;Reymbaut et al., 2021), understanding of epileptic lesions (Lampinen et al., 2020b) or multiple sclerosis (Andersen et al., 2020).

The diffusion time is another variable that can be used to sensitize the signal to different aspects of microstructure, which is defined as the time duration during which random molecular displacements are sampled (Stepišnik, 1993;Latour et al., 1994;Le Bihan, 2003). At short diffusion times, the water molecules encounter only their immediate surrounding (Mitra et al., 1993), but at longer times, they probe most of the environment (Fieremans et al., 2016;Lee et al., 2020c). By varying the diffusion time, we can probe various length-scales of tissue and, therefore, sensitize the dMRI signal to microstructural features on different length scales (Does et al., 2003;Lasič et al., 2009;Novikov et al., 2014).

Although finding microstructural features of relevance and defining new experimental approaches is challenging, addressing these two shortcomings is worthwhile because dMRI could serve as substitution for biopsy. With biopsy the tissue needs to be invasively extracted from the body, which may not be possible if it is in a difficult location. Moreover, it might be painful, may not be available and cannot be repeated on the same tissue. This is a pressing problem especially in conditions affecting the brain, as in the case of intracranial tumors. Taken together, there is in the clinics a need for non-invasive estimates of specific tumor and white matter microscopic features that would inform diagnosis, classification, prognosis or treatment response. If the shortcomings of conventional dMRI can be solved, it will be valuable for a wide range of applications where the configuration of tissue microstructure is relevant.

The aim of this thesis is to address two gaps in knowledge. The first gap concerns how larger-scale arrangements of microstructural features, sometimes referred to as mesoscopic properties, influence dMRI in cancer and axons in white matter. Current interpretations tend to rely on singular features such as cell density (in cancer) or simple models of axons such as straight-cylinders (white matter). Tissue features on the mesoscopic level, such as heterogeneity in cancer or long-range geometrical aspects of axons, have been insufficiently investigated. The second gap concerns so-called tensor-valued dMRI. It is a relatively new method for dMRI encoding. Its benefits for microstructure modelling are today well established, but it is still unknown how this translates into benefits for medical science or clinical practice. Evaluating this could pave the way for the adoption of a new generation of diffusion MRI experiments, microstructure models and encoding schemes.

2. Aims

Our first set of aims concerned how mesoscopic variations of tissue influence the macroscopic dMRI observables. These aims were:

1. In Paper I, to identify mesoscopic model parameters that are relevant from the time-dependent dMRI measurement perspective in synthetic simulations. We aimed to find which features of non-straight axons are observable with clinically achievable diffusion encoding schemes and whether axonal undulations could lead to misinterpretation of results based on approaches modelling axons as straight cylinders.
2. In Paper II, to investigate which microstructural features in meningioma tumors that account for the variations in the dMRI parameters. We focused on the mesoscopic level, and whether structures such as cell packings, collagen fibers or tissue anisotropy affect the interpretations of variations in mean diffusivity and fractional anisotropy.

Our second set of aims was tied to the gap in knowledge about potential contributions of tensor-valued diffusion MRI in imaging of intracranial tumors. These aims were:

3. In Paper III, to investigate what information can be gleaned from tensor-valued diffusion encoding in glioma tumors without the application of any modelling. We investigated whether diffusion-weighted imaging obtained by spherical b-tensor encoding (STE) can be used to suppress white matter and enhance the conspicuity of glioma hyperintensities unrelated to white matter.
4. In Paper IV, to investigate whether we can execute a protocol with tensor-valued diffusion encoding fast in the context of a clinical study and to characterize the iso- and anisotropic kurtoses in a wide range of intracranial tumors.
5. In Paper V, to evaluate whether tensor-valued dMRI can bring benefits to the preoperative prediction of meningioma consistency, grade or type in comparison with conventional diffusion tensor and kurtosis imaging.

3. Biological substrate

3.1. Intracranial tumors

Cancer is a family of diseases that is characterized by uncontrollable cell growth that often spreads from the initial site to other parts of the body. It is the first or second leading cause of death before the age of 70 years in 112 of 183 countries and ranks third or fourth in further 23 countries (Sung et al., 2021).

Tumors of the central nervous system contribute with 2.5 % to the overall number of cancer deaths (Sung et al., 2021). They can be classified based on the WHO classification from year 2016 (Louis et al., 2016) which was updated in 2021 (Louis et al., 2021). The most common primary intracranial tumors are meningiomas (36 %) and gliomas (25 %).

In this chapter, an overview of these two types of intracranial tumors will be provided. Common symptoms, treatment, radiological and histological appearance, and survey unsolved problems will also be described.

3.1.1. Meningiomas

Meningiomas are intracranial tumors that stem from the meninges. They have an annual incidence rate of approximately 8 in 100,000 (Wiemels et al., 2010) and are divided into 15 different histological types (Louis et al., 2021). Although meningiomas are predominately benign, they often necessitate neurosurgical resection because of their impact on the surrounding tissue (Maggio et al., 2021). Therefore, pre- and postoperative assessment and radiological differential diagnosis are of importance.

Most meningiomas are asymptomatic and are therefore found incidentally. Larger tumors, especially with adjacent oedema, may present themselves as a headache, paresis, change in mental status, as well as more specific symptoms related to their location (Greenberg et al., 1999).

Diagnostically, meningiomas often appear as dural masses that are isointense on T1- and T2-weighted images but enhancing with respect to white matter. Nonetheless, microcystic or angiomatous subtypes of meningiomas with respect to atypical (grade II or III) meningiomas may pose a diagnostic challenge. That

notwithstanding, dMRI has shown potential in differentiating between the subtypes (Jolapara et al., 2010;Xiaoai et al., 2020).

Estimation of their consistency, which is defined as the mechanical firmness of the tumor tissue, is of importance pre-operatively (Shiroishi et al., 2016;Yao et al., 2018). This is because soft tumors are associated with lower surgical morbidity, shorter operative time, and lower rates of recurrence (Yao et al., 2018), and thereby its knowledge has an impact on the neurosurgical resection strategy. T2-weighted MRI (Yao et al., 2018), MR elastography (Chartrain et al., 2019) and DTI (Kashimura et al., 2007;Romani et al., 2014) provide a useful predictive measure of tumor consistency but no method is widely established.

Finally, meningiomas are interesting not only clinically but also scientifically in investigations of mesoscopic variations of tissue because the meningioma types are highly heterogeneous. Thus, collecting different sample types is of interest because these may span a large tissue variability and different realization of mesoscopic variability.

3.1.2. Gliomas

Gliomas comprise a wide range of tumors originating from glial cells in the brain or spine. They make up approximately 80 % of malignant brain tumors and can be divided based on their cell type, grade or location (Louis et al., 2021). The most common three types are glioblastoma, oligodendroglioma and astrocytoma. They often manifest themselves non-specifically by headaches, seizures, vomiting but also more specifically depending on their anatomic location. Their treatment and survival rate depends on the subtype but for the most common subtype, i.e. glioblastomas, which is only 5 % (Ricard et al., 2012).

Histologically, the appearance of gliomas varies among the different types and grades, but low-grade gliomas are often composed of groups of scattered cells infiltrating the surrounding brain (Kumar et al., 2017). High-grade gliomas, on the other hand, often have a central core of a more or less compact tumor with a border pushing against and compressing the surroundings.

Radiologically, glioblastomas appear as large tumors at diagnosis and often have thick, enhancing margins and a central necrotic core surrounded by vasogenic oedema, which usually contains infiltration by neoplastic cells (Brant and Helms, 2012). On diffusion-weighted imaging, localized high-signal values relative to the surrounding are often seen, often referred to as tumor-related hyperintensities. Their presence is indicative of prognosis (Kolakshyapati et al., 2017), perhaps because they are linked to increased cell density (Chen et al., 2013;LaViolette et al., 2014). On high b-value DWI (b = 2,000–3,000 s/mm^2) the hyperintensities are more conspicuous, more useful for discriminating high- and low-grade gliomas (Seo et al., 2008), and better for the prediction of overall survival for patients with

glioblastomas (Zeng et al., 2018). These, however, may be confounded by white matter because white matter also appears hyperintense at high *b*-value DWI. One of the open clinical problems is their delineation because they spread beyond enhancements on post-gadolinium T1w images. In summary, there is a need for radiological stratification that can prognosticate survival and correlate with the WHO classification (Kamble et al., 2022).

3.2. Neurons and axons

Neurons or nerve cells are cells that receive and process electrochemical stimulations that are further conveyed to other cells. They are the main component of nervous tissue and typically consist of soma (neuronal body) from which dendrites and single axon are extruding (Figure 1A). Dendrites are filaments that receive electrochemical stimulations from other cells. They may solely transfer the signal, control glands or muscles or process inputs from sensory organs.

Axons are analogous to wires that connect various parts of the brain. They are projections of neurons that propagate the signal from the soma by controlling the ion concentration across ion channels embedded in the cytoplasmatic membrane called axolemma (Clark et al., 2010).

One key functional part of the axon is its myelin sheath, which is an extrusion of oligodendrocytes consisting of lipids (Figure 1B). It plays a crucial role because it increases the conduction velocity. Myelin is not a continuous surface but is interrupted by so-called nodes of Ranvier. The myelin wraps around the axolemma in multiple folds (Edgar and Griffiths, 2009), and between these folds water is trapped (Hildebrand et al., 1993). This means that this water is highly restricted and not permeable, at least not for diffusion times that are typical for clinical dMRI.

Axons are characterized by their diameter, which is important because it is also linked to the conduction velocity (Ritchie, 1982). The axon diameters vary within tracts as well as within individual axons (Figure 1B). In the corpus callosum, the axon diameters are in range between 0.5 and 15 μm, but the volume-weighted average is below 1 μm (Aboitiz et al., 1992). This was also observed with 3D morphometry studies of axons by electron microscopy that found that the median of the equivalent diameter in a corpus callosum is around 0.5 μm (Abdollahzadeh et al., 2019;Lee et al., 2019), with a median coefficient of variation of 4 (Lee et al., 2019) or interquartile range of 0.35 μm – 0.55 μm (Abdollahzadeh et al., 2019) (Figure 1D). The equivalent diameter is defined as a diameter of a circle with the same area as the cross-section excluding the myelin sheath perpendicular to the axon skeleton. The axon diameters may also vary between different nerves; for example, in optic nerve, the typical diameter is around 1 μm (Jonas et al., 1990;Jeffery, 1996), and or in phrenic nerve it is around 5 μm (Takagi et al., 2009). Finally, the axon

cross section is rather elliptic rather than circular (Abdollahzadeh et al., 2019;Lee et al., 2019) with a median ellipse eccentricity in the corpus callosum above 0.65 (Abdollahzadeh et al., 2019).

Axons do not propagate straight but exhibit non-straight—often sine-like—trajectories, referred to as undulations (Figure 1C), which are present in both the central (corpus callosum or optic nerve) and peripheral nervous system (phrenic nerve). They may be relevant functionally in tissue mechanics because they may be stretched or compressed in the hydrocephalus or by a tumor (Bain et al., 2003).

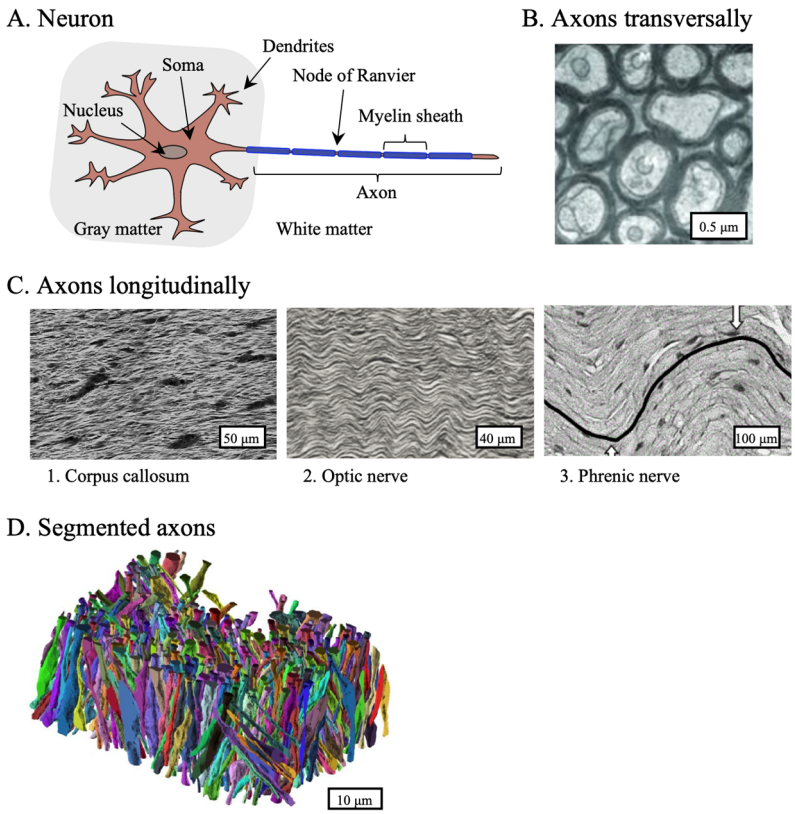

Figure 1. Neurons and their projections-axons. Panel A shows a neuron. It consists of the soma (body) that is in the gray matter. From the soma dendrites extrude within the gray matter and a single axon to white matter. Myelin sheaths wrap around the axon. Panel B shows cross-sections of axons in an electron microscopy image in a transversal plane of a mouse optic nerve. The darker regions correspond to myelin sheaths. Panel C shows that axons in the longitudinal plane exhibit sine-like trajectories, referred to as undulations. These are ubiquitous in the central nervous system, for example in the corpus callosum (C1) or optic nerve (C2) but also in the peripheral nervous system, for example in the phrenic nerve (C3). Panel D shows segmented axons (without myelin sheaths) from a series of electron microscopic images in the corpus callosum. Axons are not only undulating, but they also have different orientation dispersions or variable intra- and inter-axon diameters, features that may need to consideration when modelling the axons. Panel B adapted from Stassart et al. (2018), published by Frontiers Media and licensed under CC BY 4.0. Panel C1 was adapted, with permission, from Schilling et al. (2018), published by Elsevier. Panel C2 was adapted, with permission, from Jeffery (1996), published by Wiley. Panel C3 was adapted, with permission, from Lontis et al. (2009), published by © 2011 IEEE. Panel D was adapted, with permission, from Lee et al. (2019), published by Springer Nature.

3.3. Histology

Histology studies the anatomy of tissues at the microscopic level, often by using microscopes. It concerns itself with different organs, the study of cells (cytology) or of pathological variations (histopathology) (Mescher, 2021).

Before tissue observation, the sample needs to be prepared. First, a representative sample needs to be selected and extracted. Second, the tissue sample needs to be fixated, which means that the biochemical reactions that would otherwise lead to self-degradation needs to be stopped. The most used fixative is formalin, which is a solution of formaldehyde. Third, the sample needs to be embedded in a harder medium that allows it to be cut into thin layers. This is often achieved by the use of paraffin. Because paraffin wax is not mixable with water the tissue needs to be dehydrated before embedding, which is achieved with ethanol. When the wax cools down the sample can be sectioned into 4-15 μm thin slices.

To emphasize specific microstructural features, various stains are available. The most common stain that provides overview is Hematoxylin and Eosin (H&E or HE). The hematoxylin stains cell nuclei with a purple color, whereas eosin attaches to the extracellular matrix and cytoplasm and gives them a pink color. Other structures have different color tones of the combination of purple and pink. Another widely used stain is the Nissl stain that attaches to genetic material (nuclear chromatin) through the use of cresyl violet acetate or toluidine blue. This stain, when applied in nervous tissue, highlights neuronal bodies.

4. Diffusion in tissue

Diffusion MRI probes diffusion due to the random motion of molecules, often referred to as Brownian motion or self-diffusion (Einstein, 1905). A key feature characterizing diffusion is the diffusion coefficient D defined as a ratio between mean squared displacement, $\langle \Delta \mathrm{x}^2(t_\mathrm{D}) \rangle$, and the diffusion time, t_D, which is the time duration during which random spin displacements are sampled (Stepišnik, 1993;Latour et al., 1994),

$$D = 2 \cdot \frac{\langle \Delta \mathrm{x}(t_D)^2 \rangle}{t_D} = 2 \cdot \frac{\langle \left(\mathrm{x}(t_D - t_0) - \mathrm{x}(t_0)\right)^2 \rangle}{t_D}, \tag{4.1.1}$$

where t_0 is the starting time, $\mathrm{x}(t)$ is the position of the spin-bearing particle at time t, D is the diffusion coefficient and $\langle \cdot \rangle$ the average across all Brownian spin trajectories. In tissue, the diffusion coefficient D is lower than what would otherwise be measured in a free medium because displacements are hindered by microstructural features. This is the reason why it is referred as an apparent diffusion coefficient (ADC).

To study how microstructure influences the mean squared displacement and the ADC, we may distinguish between three distinct types of diffusion regimes: free, restricted and hindered. These characteristics may be same across all directions, and then it is referred to them as isotropic. If they differ in any direction, they are referred to as anisotropic. The different types of diffusion are linked to three different types of environments and by studying the effects on the apparent diffusion coefficient, i.e. ADC as a function of diffusion time $\mathrm{ADC}(t_\Delta)$ and ADC as a function of direction $\mathrm{ADC}(\mathbf{u})$, we could separate them (Figure 2).

- Free diffusion arises in an environment that has barriers separated by a distance d that is much larger than maximal mean squared displacement, $d \gg \sqrt{\langle \Delta \mathrm{x}^2 \rangle}$ (Figure 2A). There are effectively no obstacles for the diffusing particles, so the mean squared displacement is given by reverting the Eq. 4.1.1 and the ADC is constant as the diffusion time is varied.
- Restricted diffusion arises in an environment within impermeable barriers of size d, which prohibits the diffusing particles to escape (Figure 2B). The mean squared displacement is, at shorter diffusion times when $d \gg \sqrt{\mathrm{D}_0 t_D / 2}$, linearly increasing according to Eq. 4.1.1. At longer diffusion

times, when $d \ll \sqrt{\mathrm{D}_0 t_D/2}$, the apparent diffusion coefficient ADC tends to 0 because $ADC \approx \mathrm{const}/(2t_D) \to 0$ as $t_D \to \infty$. In the Figure 2B, the diffusion is restricted along y-axis but free along x-axis.

- Hindered diffusion arises in an environment with obstacles at a distance shorter than the mean squared displacement, $d \ll \sqrt{\mathrm{D}t_D/2}$ (Figure 2C). The obstacles are hindering ("slowing") the diffusing particles. The mean squared displacement in the long-time limit when $d \ll \sqrt{\mathrm{D}t_D/2}$ is described by Eq. 4.1.1 but because the particles appear to be diffusing at a slower pace, the diffusion coefficient D_0, which would normally correspond to free diffusion and is referred to as bulk diffusion coefficient, is replaced by lower ADC. The ratio by which the diffusion is hindered is called tortuosity, $\lambda^2 = ADC/D_0$. On the other hand, at very short diffusion times, $\langle \Delta \mathrm{x}^2 \rangle$ and ADC behave as free diffusion because only a minority of particles sense the obstacles (Mitra et al., 1993), i.e. ADC = D_0.

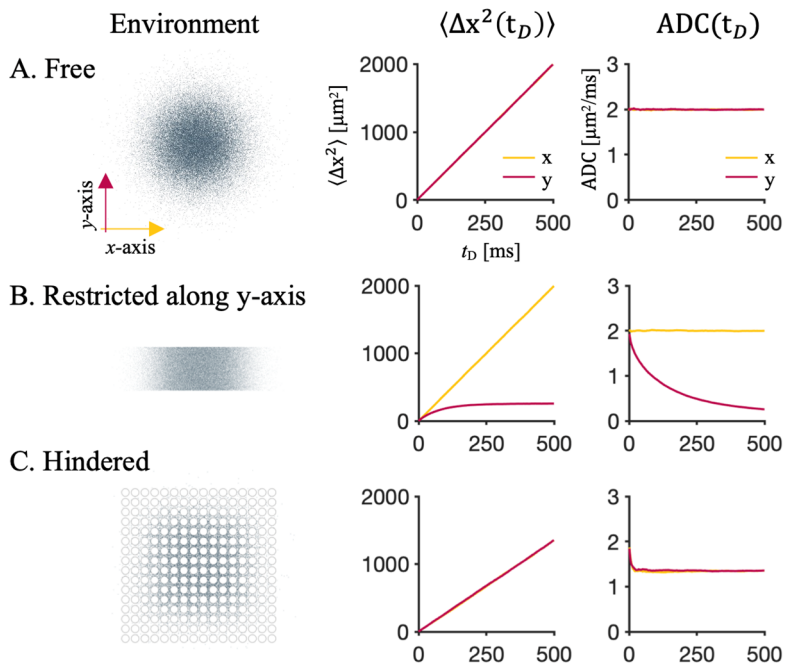

Figure 2. Free, restricted and hindered diffusion. Panel A shows free diffusion, which is characterized by a linear mean squared displacement (MSD) and a constant ADC. Panel B shows restricted diffusion between two planes along the y-axis. The restricted diffusion along this axis is characterized by increasing but bounded MSD and monotonically decreasing ADC. Panel C shows hindered diffusion by circular impermeable restrictions and is characterized by linearly increasing MSD and constant ADC except for low diffusion times. By incorporating measurements at variable diffusion times and measuring the diffusion along orthogonal directions, we can separate the case A, B and C. Diffusion simulated using the diffusion coefficient of water at 20° C, i.e. D_0 = 2 μm²/ms, and simulation is available at https://github.com/jan-brabec/kappa.

In summary, the microstructure leaves an imprint on the diffusion. The relevant length-scale for clinical dMRI is in the units of micrometers, because the square root of mean squared displacement ($\sqrt{\langle \Delta x^2 \rangle}$) is in the range of micrometers. Specifically, it is between 3 μm and 55 μm assuming diffusion times of t_D = 8-500 ms at the clinical scanner (Clark et al., 2001;Does et al., 2003) and a diffusion coefficient of free water D = 3 μm^2/ms at a body temperature of 37 °C (Mills, 1973). Structures on this length scale will hence have an impact of the diffusion observed by clinical dMRI. However, the image voxel volumes are typically around 2×2×2 mm^3, which means that dMRI does not measure individual features but rather an averaged across a large number of microenvironments.

5. Diffusion encoding and modelling

Diffusion encoding is performed by the application of a series of time-dependent magnetic field gradients that impose patterns of spin phase modulations. This modulation leads to a signal loss that, in turn, can be related to diffusion. The particular choice of diffusion encoding is important because it influences what diffusional, and therefore microstructural, properties, are encoded into the signal.

The obtained signal values can be turned into dMRI parameters by modelling. The diffusion-weighted signal **S** is obtained for given model parameters **p** and diffusion encoding **e** which referred to as the forward problem,

$$\mathbf{S} = f(\mathbf{p}, \mathbf{e}), \tag{5.1.1}$$

where f is a general mapping function of various forms that will be described in this chapter. From the signal and encoding we can estimate the parameters by solving the so-called inverse problem,

$$\mathbf{p} = f^{-1}(\mathbf{S}, \mathbf{e}), \tag{5.1.2}$$

where f^{-1} is the inverse mapping function of f. The inverse problem is solved by finding the model parameters that are most likely generated by the observed noisy signal. In practice, this is performed by minimizing the sum-of-squares distance between observed and predicted signals.

Here, three types of encodings are introduced – conventional, tensor-valued and time-dependent. The encodings are also coupled to parameters reflecting gross features of diffusion (Eq. 5.1.1), and how to solve the inverse problem (Eq. 5.1.2) will be sketched for tensor-valued dMRI.

5.1. Conventional diffusion encoding

The most commonly used diffusion-weighted pulse sequence is formed by inserting two trapezoidal (pulsed) diffusion encoding gradients before and after the refocusing (180°) RF pulse, as depicted in Figure 3 (Stejskal and Tanner, 1965). In the conventional setup, the diffusion encoding gradients can be described by their

strength G, duration δ, and separation between the onsets of each gradient Δ, and an encoding direction $\mathbf{u}$ (in Figure 3, the direction is along gradient x, $\mathbf{u} = \mathbf{g}_x$).

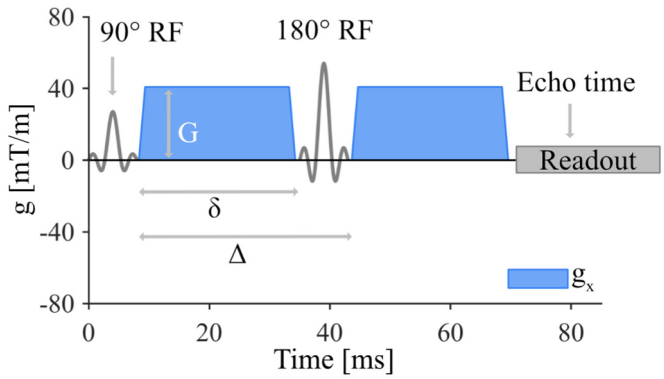

Figure 3. Scheme of the most commonly used diffusion encoding sequence (Stejskal and Tanner, 1965). It is a spin-echo diffusion encoding sequence with EPI readout. It consists of two pulsed diffusion encoding gradients placed before and after a refocusing pulse. These can be described by a diffusion gradient strength G, duration of the diffusion gradient δ, and separation between onsets of each diffusion gradient Δ.

Due to the first diffusion encoding gradient the spins acquire a phase, and by the second diffusion gradient the spins are rephased. Spins that did not move between the first and second gradient will reacquire their original phase (effects of T2 relaxation are neglected) and will thus not contribute to the signal loss. However, those spins that changed location, for example due to diffusion, do not reacquire their original phase. Specifically, the phase of a single spin at echo time TE is given by

$$\phi(TE) = \gamma \int_0^{TE} \mathbf{g}(t) \cdot \mathbf{r}(t) \mathrm{d}t, \tag{5.1.3}$$

where γ is the gyromagnetic ratio (for hydrogen γ = 42.58 MHz/T), TE is the echo time, $\mathbf{g}(t)$ is the time-varying diffusion encoding gradient, $\mathbf{r}(t)$ is the spin position at time t and $[\cdot]$ represents the dot product between two vectors.

The diffusion signal is given by averaging over all spin contributions as

$$S = \langle \exp(i\phi) \rangle. \tag{5.1.4}$$

A phase dispersion thus leads to a signal attenuation, and this is the overarching building block of dMRI, which is captured in Eq. 5.1.4. With stronger gradients or larger diffusion (Eq. 5.1.3), the signal attenuation increase, and by studying this signal loss (Eq. 5.1.4), we can infer diffusional features, which is the topic of study in this chapter.

5.1.1. Diffusion-weighted imaging (DWI)

One of the most essential applications of dMRI is so-called diffusion-weighted imaging (DWI). Loosely defined, DWI is a simple method producing images that are strongly weighted by diffusion. It also enables estimation the ADC. In practice this is often achieved by the conventional spin-echo sequence (Chapter 5.1) (Stejskal and Tanner, 1965). The apparent diffusion coefficient ADC is estimated by assuming exponential attenuation,

$$\mathrm{S}(b) = \mathrm{S}_0 \exp(-b \cdot \mathrm{ADC}), \tag{5.1.5}$$

where the *b*-value characterizes the diffusion encoding strength. It summarizes the parameters *G, δ* and Δ as

$$b = \gamma^2 \mathrm{G}^2 \delta^2 (\Delta - \delta/3), \tag{5.1.6}$$

where $(\Delta - \delta/3) = t_{\mathrm{eff}}$ is the effective diffusion time (Le Bihan, 2003). If the diffusion is free, the apparent diffusion coefficient is actually the bulk diffusion coefficient, ADC = D_0. The maximum *b*-value should not be set too high (often it is set to $b = 1000$ s/mm^2), otherwise ADC may be biased due to non-mono-exponential attenuation (Jones and Basser, 2004).

Figure 4 shows a patient of age around 50 years, who had an astrocytoma of grade II. On the contrast-enhanced T1w image (T1w + Gd), an enhancing lesion can be seen (marked with a yellow arrow). On a map obtained without diffusion encoding (S_0), a hyperintense region surrounding the enhancing lesion can also be seen. However, on the DWI at $b = 1400$ s/mm^2 a bright hyperintense lesion that is not visible on the S_0 map can be observed (also marked by a yellow arrow). The ADC can be averaged across several directions and a mean diffusivity (MD) can be obtained. The MD map of the patient shows a slight relative decrease in the corresponding region.

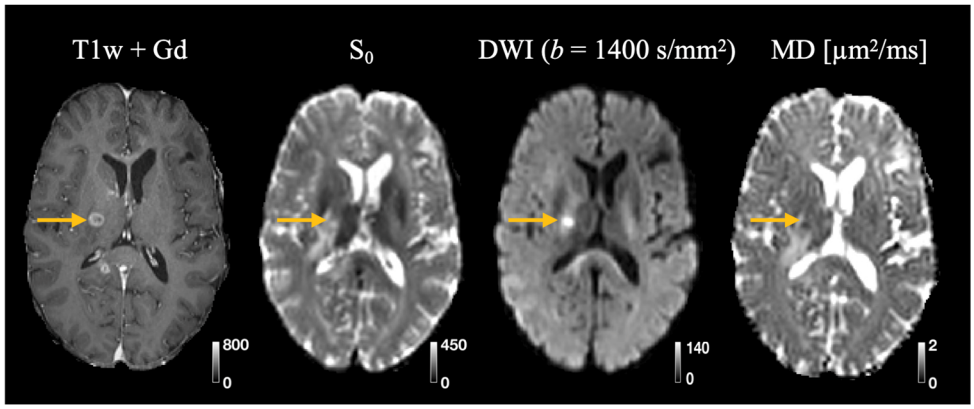

Figure 4. MRI in a patient with an astrocytoma of grade II. On the contrast-enhanced T1w image, an enhancing lesion can be seen (marked with a yellow arrow). On a map obtained without diffusion encoding (S_0), a hyperintense region can also be seen. However, on the DWI scan at b = 1400 s/mm^2 a hyperintense lesion can be seen that is not visible on the S_0 map. The MD map shows a slight relative decrease of the MD in the corresponding region. Figure adapted from Paper III, published by Frontiers Media and licensed under CC BY 4.0.

5.1.2. Diffusion tensor imaging (DTI)

If the diffusion encoding is performed in several directions, diffusion tensor imaging (DTI) can be used to probe the voxel-averaged diffusion anisotropy (Basser et al., 1994;Basser and Pierpaoli, 2011). In essence, it generalizes the concept of the diffusion coefficient (scalar) into a notion of a diffusion tensor **D**,

$$\mathbf{D} = \begin{pmatrix} D_{\mathrm{xx}} & D_{\mathrm{xy}} & D_{\mathrm{xz}} \\ D_{\mathrm{yx}} & D_{\mathrm{yy}} & D_{\mathrm{yz}} \\ D_{\mathrm{zx}} & D_{\mathrm{zy}} & D_{\mathrm{zz}} \end{pmatrix}. \tag{5.1.7}$$

The diffusion tensor **D** has 6 degrees of freedom due to symmetry ($D_{ij} = D_{ji}$). The ADC from DWI is given by the projection of the diffusion tensor onto an encoding direction **u**, i.e. $ADC = \mathbf{u}^{\mathbf{T}} \cdot \mathbf{D} \cdot \mathbf{u}$, and the signal can be written as

$$\mathrm{S}(\mathbf{u}, b) = \mathrm{S}_0 \exp\left(-b \cdot \mathbf{u}^{\mathbf{T}} \cdot \mathbf{D} \cdot \mathbf{u}\right). \tag{5.1.8}$$

It is possible to diagonalize the tensor **D** such that $\mathbf{D} = \mathbf{R}\boldsymbol{\Lambda}\mathbf{R}^{-1}$ where $\boldsymbol{\Lambda}$ is the diagonal representation $\boldsymbol{\Lambda}$ of **D** (Basser et al., 1994),

$$\boldsymbol{\Lambda} = \begin{pmatrix} \lambda_1 & 0 & 0 \\ 0 & \lambda_2 & 0 \\ 0 & 0 & \lambda_3 \end{pmatrix}, \tag{5.1.9}$$

and **R** the rotation matrix (Kingsley, 2006). From the eigenvalues (λ_1, λ_2, λ_3) we can define parameters, such as mean diffusivity (MD),

$$\mathrm{MD} = \frac{\mathrm{Tr}(\mathbf{D})}{3} = \frac{\lambda_1+\lambda_2+\lambda_3}{3}, \tag{5.1.10}$$

where Tr[·] is the trace of the tensor, and fractional anisotropy (FA) as

$$\mathrm{FA} = \sqrt{\frac{3}{2}} \cdot \sqrt{\frac{(\lambda_1-\mathrm{MD})^2+(\lambda_2-\mathrm{MD})^2+(\lambda_3-\mathrm{MD})^2}{\lambda_1^2+\lambda_2^2+\lambda_3^2}}. \tag{5.1.11}$$

Note that MD and FA are orientation-independent voxel-level measures, where MD reflects the average diffusion across directions and FA reflects the anisotropy of the diffusion tensor.

DTI necessitates diffusion data acquired at sufficiently low *b*-values where the signal decay is approximately exponential, often with *b*-values up to 1000 s/mm^2. It also demands diffusion encoding in at least 6 directions, although 15 or more directions are recommended (Jones et al., 2013). At high *b*-values higher order terms may bias the estimates of MD and FA because DTI assumes mono-exponential decay of the diffusion signal (Eq. 5.1.8).

5.1.3. Diffusion kurtosis imaging (DKI)

To characterize the signal at higher *b*-values (over 1000 s/mm^2), where the decay is not mono-exponential, so-called diffusion kurtosis imaging can be used (DKI) (Jensen et al., 2005). DKI yields a parameter termed mean kurtosis (MK). This can be obtained by fitting the diffusion-signal with (Yablonskiy and Sukstanskii, 2010)

$$\bar{S}(b) = \exp\left(-b \cdot \mathrm{MD} + \frac{1}{6} b^2 \cdot \mathrm{MD}^2 \cdot \mathrm{MK}\right). \tag{5.1.12}$$

Note that the Eq. 5.1.12, which contains signal averaged across several directions is a modification of the DKI model proposed by Jensen et al. (2005). The non-mono-exponential signal, which leads to a non-zero MK, may be due to several reasons (De Swiet and Mitra, 1996). One reason is tissue heterogeneity within the image voxel due to the presence of environments with distinct diffusivities. Another is anisotropy and orientation dispersion, and tensor-valued encoding may be useful in this situation (Chapter 5.2). Yet another reason is the presence of obstacles that lead to time-dependence of the diffusion, which is arises at intermediate diffusion times where ADC cannot be regarded as constant. Here, time-dependent encoding may helpful (Chapter 5.3).

5.2. Tensor-valued encoding

The concept of a *b*-value as a measurement variable can be generalized into a b-tensor (Westin et al., 2016). The b-tensor can be represented by the conventional *b*-value but in addition also the b-tensor shape, or b_Δ. Importantly, this parameter provides a complementary contrast to the conventional *b*-value. The b-tensor formalism is appealing because it allows a compact description of many seemingly different experiments, such as those using numerically optimized free gradient waveforms (Sjölund et al., 2015;Szczepankiewicz et al., 2021a), double diffusion encodings (Cory et al., 1990;Callaghan and Komlosh, 2002;Özarslan and Basser, 2008;Lasič et al., 2011;Jespersen et al., 2013;Lawrenz and Finsterbusch, 2013;Shemesh et al., 2016) or isotropic diffusion encoding used in the context of fast MD mapping (Mori and Van Zijl, 1995;Wong et al., 1995). The b-tensor is defined from the gradient waveform as (Mattiello et al., 1994;Westin et al., 2016)

$$\mathbf{B} = \int_0^{TE} \mathbf{q}(t)^{\otimes \mathbf{2}} \mathrm{d}t = \int_0^{\mathrm{TE}} \mathbf{q}(t)\mathbf{q}(t)^{\mathrm{T}} \mathrm{d}t, \tag{5.2.1}$$

where $\mathbf{q}(t) = \gamma \int_0^t \mathbf{G}(t')\mathrm{d}t'$ and $\mathbf{G}$ is the gradient. The symbol '$\otimes$' denotes the outer product between two tensors of order *m*, and *n* yields a tensor of order *m*+*n* with elements that are different product combinations between the elements of the two tensors such that $(\mathbf{X} \otimes \mathbf{Y})_{ijkl} = X_{ij}Y_{kl}$.

If $\mathbf{B}$ is axisymmetric, it can be expressed in its principal axis system (PAS) in terms of its axial ($b_\parallel$) and radial ($b_\perp$) eigenvalues,

$$\mathbf{B}_{\mathrm{PAS}} = \begin{pmatrix} b_\parallel & 0 & 0 \\ 0 & b_\perp & 0 \\ 0 & 0 & b_\perp \end{pmatrix}. \tag{5.2.2}$$

The B-tensor is given by $\mathbf{B} = \mathbf{R} \cdot \mathbf{B}_{\mathrm{PAS}} \cdot \mathbf{R}^{\mathbf{T}}$ where $\mathbf{R}$ is a rotation matrix (Kingsley, 2006), and the *b*-value, describing the encoding strength, is the trace of the B-tensor,

$$b = \mathrm{Tr}(\mathbf{B}) = b_\parallel + 2b_\perp, \tag{5.2.3}$$

whereas b-tensor shape, b_Δ, is defined as (Eriksson et al., 2015)

$$b_\Delta = \frac{b_\parallel - b_\perp}{3b}, \tag{5.2.4}$$

where b_Δ can assume values from –0.5 (referred to as planar b-tensor encoding or PTE), through 0 (spherical b-tensor encoding or STE) to 1 (linear or LTE). The

definition of b-tensors (Eq. 5.2.1), together with a parametrization by the *b*-value (Eq. 5.2.3) and b-tensor shape (Eq. 5.2.4), defines a family of b-tensors (Figure 5A).

Different gradient waveforms can generate identical b-tensors. For example, linear b-tensors (LTE; b_Δ=1) can be generated by the conventional diffusion experiment (Stejskal and Tanner, 1965) (Figure 3) as well as by a free gradient waveform. Similarly, there are several ways to generate spherical b-tensors (Szczepankiewicz et al., 2021b) where one of such way is magic-angle spinning of the q-vector (qMAS) (Eriksson et al., 2013). This approach was used in earlier studies (Westin et al., 2016), whereas our studies (Paper III; Paper IV; Paper V) used numerically optimized gradient waveforms (Sjölund et al., 2015;Szczepankiewicz et al., 2019b;Szczepankiewicz et al., 2021b). Gradient waveforms similar to the one shown in Figure 5B were used in our studies Paper III, Paper IV and Paper V.

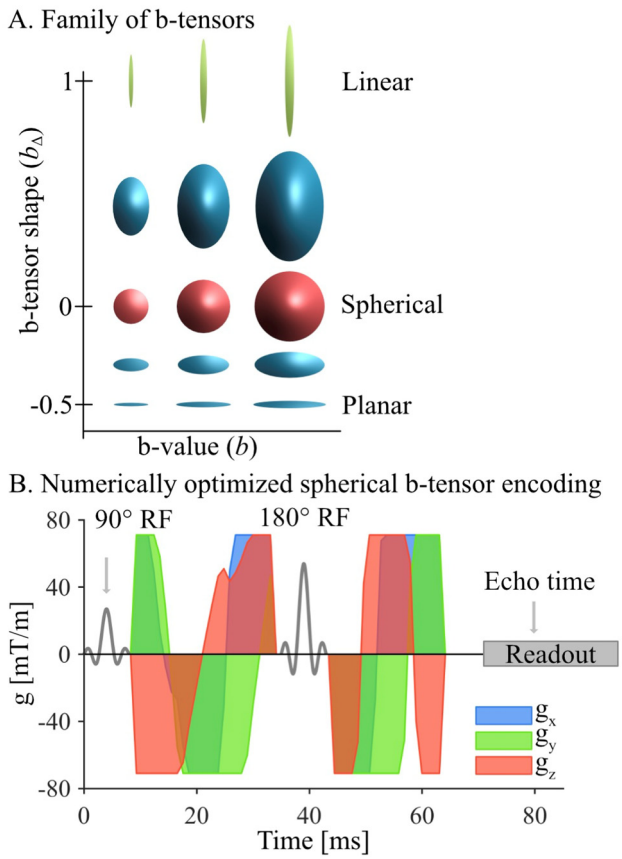

Figure 5. B-tensor types and encoding. Panel A shows the family of b-tensors that can be parameterized by two variables – the b-tensor shape and the *b*-value. Panel B shows an example of numerically optimized gradient waveforms that leads to spherical b-tensor encoding (b_Δ = 0) (Sjölund et al., 2015;Szczepankiewicz et al., 2019b;Szczepankiewicz et al., 2021b). Similar waveforms were used in our studies Paper III, Paper IV and Paper V.

5.2.1. Q-space trajectory imaging (QTI)

Tensor-valued encoding can be connected to a representation of diffusion in tissue that is termed the diffusion tensor distribution (DTD) (Jian et al., 2007;Westin et al., 2016). With the DTD, the diffusion process is represented by a distribution of diffusion tensors **D** and not only by a single voxel-averaged diffusion tensor $\langle \mathbf{D} \rangle$. Importantly, a single voxel-averaged diffusion tensor can correspond to multiple distinct DTDs. The environments connected to individual diffusion tensors are assumed to be non-exchanging and results may be biased if diffusion-time dependence is present, which can be regarded as limitations of this approach.

A DTD can describe tissue heterogeneity because it represents the tissue as multi-gaussian, i.e., as a diffusion originating from multiple compartments that may vary with respect to their diffusivities or anisotropies at the microscopic level within a single image voxel. Based on this concept, it can be shown that the mean kurtosis (MK) from DKI can be disentangled into anisotropic and isotropic diffusional kurtoses, $\mathrm{MK_A}$ and $\mathrm{MK_I}$, respectively, that are informing on different aspects of diffusion (Szczepankiewicz et al., 2016). Whereas $\mathrm{MK_A}$ reflects microscopic tissue anisotropy, $\mathrm{MK_I}$ rather reflects cell density variation (Szczepankiewicz et al., 2016). However, to estimate these, measurements with at least two different b-tensor shapes are needed, and we will refer to tensor-valued encoding alongside the DTD model for the purpose of decomposing MK into $\mathrm{MK_A}$ and $\mathrm{MK_I}$ as Q-space imaging (QTI).

The DTD can be described by several marginal distributions or parameters. One such is a distribution of isotropic diffusivities D_I defined as (Westin et al., 2016)

$$D_\mathrm{I} = \mathrm{E}_\lambda[\mathbf{D}], \tag{5.2.5}$$

where operator $\mathrm{E}_\lambda[\cdot]$ yields a scalar that is the average across the tensor eigenvalues in 3 dimensions as $\mathrm{E}_\lambda[\mathbf{X}] = \frac{1}{3}\sum_{i=1}^{3} \lambda_i$. This operator can be applied to the distribution, and then it yields a distribution of scalars. For completeness, the mean diffusivity (MD) can be defined from the voxel-level average $\langle \mathbf{D} \rangle$ as

$$\mathrm{MD} = \mathrm{E}_\lambda[\langle \mathbf{D} \rangle] = \langle \mathrm{D_I} \rangle. \tag{5.2.6}$$

Both MD and D_I represent mean diffusivities but are different. Whereas MD represents at the voxel-level, D_I can be considered as the distribution of MD within the image voxel.

The isotropic variance of the DTD is defined as

$$\mathrm{V_I} = \langle \mathrm{E}_\lambda[\mathbf{D}]^2 \rangle - \mathrm{E}_\lambda[\langle \mathbf{D} \rangle]^2, \tag{5.2.7}$$

whereas anisotropic variance is defined as

$$\mathrm{V_A} = \frac{2}{5}\langle \mathrm{V_\lambda}[\mathbf{D}]\rangle, \tag{5.2.8}$$

where operator $\mathrm{V_\lambda}[\cdot]$ is the variance across tensor eigenvalues, $\mathrm{V_\lambda}[\mathbf{X}] = \frac{1}{3}\sum_{i=1}^{3}(\lambda_i - \mathrm{E_\lambda}[\mathbf{X}])^2$.

The two parameters $\mathrm{V_I}$ and $\mathrm{V_A}$ reflect different aspects of the DTD. The isotropic variance of the DTD (Eq. 5.2.7) reflects the variance of the isotropic diffusivities, whereas the anisotropic variance (Eq. 5.2.8) yields the average variance of the eigenvalues. The anisotropic diffusivity is zero only if all environments are isotropic in their diffusion. These distinct variances can be rescaled to yield $\mathrm{MK_E}$, $\mathrm{MK_I}$ and $\mathrm{MK_A}$ as (Szczepankiewicz et al., 2016)

$$\mathrm{MK_I} = 3\frac{\mathrm{V_I}}{\mathrm{MD}^2}, \tag{5.2.9}$$

$$\mathrm{MK_A} = 3\frac{\mathrm{V_A}}{\mathrm{MD}^2}, \tag{5.2.10}$$

$$\mathrm{MK_E} = \mathrm{MK_I} + b_\Delta^2 \cdot \mathrm{MK_A}, \tag{5.2.11}$$

where $\mathrm{MK_E}$ is termed effective kurtosis. Note that the $\mathrm{MK_E}$ depends on the value of b-tensor shape and by setting $b_\Delta = 1$ (LTE), it yields total kurtosis, $\mathrm{MK_T} = \mathrm{MK_I} + \mathrm{MK_A}$ (Lasič et al., 2014;Szczepankiewicz et al., 2016).

Using the QTI formalism, the fractional anisotropy can be defined in an alternative way to Eq. 5.1.11 according to (Lasič et al., 2014;Szczepankiewicz et al., 2016;Westin et al., 2016)

$$\mathrm{FA} = \sqrt{\frac{3}{2}}\cdot\sqrt{\frac{\langle \mathrm{V_\lambda}[\langle\mathbf{D}\rangle]\rangle}{\langle \mathrm{E_\lambda}[\langle\mathbf{D}\rangle]^2 + \mathrm{V_\lambda}[\langle\mathbf{D}\rangle]\rangle}} = \sqrt{\frac{3}{2}}\cdot\left(1 + \frac{\mathrm{MD}^2}{\frac{5}{2}\mathrm{V_\lambda}[\mathbf{D}]}\right)^{-\frac{1}{2}}. \tag{5.2.12}$$

Similarly, one can also define microscopic fractional anisotropy (μFA) as a measure of anisotropy at a microscopic level as follows (Jespersen et al., 2013;Lasič et al., 2014;Szczepankiewicz et al., 2015;Westin et al., 2016):

$$\mu\mathrm{FA} = \sqrt{\frac{3}{2}}\cdot\sqrt{\frac{\langle \mathrm{V_\lambda}[\mathbf{D}]\rangle}{\langle \mathrm{E_\lambda}[\mathbf{D}]^2 + \mathrm{V_\lambda}[\mathbf{D}]\rangle}} = \sqrt{\frac{3}{2}}\cdot\left(1 + \frac{\mathrm{MD}^2}{\frac{5}{2}\mathrm{V_A}}\right)^{-\frac{1}{2}}. \tag{5.2.13}$$

The FA (Eq. 5.2.12) and μFA (Eq. 5.2.13) differ only by order of averaging. The first is based on the eigenvalue variance of the average of the local diffusion tensors, while the second is based on the average of the local diffusion tensor eigenvalue variance. This means that FA represents voxel-level metric of anisotropy whereas μFA reflects anisotropy at the microscopic level. This also means that FA is conflated with orientation dispersion of the microscopic compartments (Szczepankiewicz et al., 2015). We can analyze microscopic anisotropy by μFA or MK_A, because they both reflect anisotropic variance V_A although they do not have the same absolute value (compare right hand side of Eq. 5.2.13 and definition of MK_A in Eq. 5.2.10).

Finally, we consider the forward model of the signal. This can be obtained by cumulant expansion of the phase distribution that is terminated at the fourth cumulant. In the absence of net flow the first and third cumulants are zero (Kiselev, 2010), and thereby the signal is given by the sum of second and fourth cumulant as

$$S(\mathbf{B}) = \mathrm{S}_0 \exp\left(-\mathbf{B} : \langle \mathbf{D} \rangle + \frac{1}{2}\mathbf{B}^{\otimes 2} : \mathbb{C}\right), \tag{5.2.14}$$

where symbol ":" denotes the double inner product that is defined as a sum over all element-wise products between two tensors, $\mathbf{X} : \mathbf{Y} = \sum_{i=1}^{3}\sum_{j=1}^{3} X_{ij}Y_{ij}$. $\mathbb{C} = \langle \mathbf{D}^{\otimes 2} \rangle - \langle \mathbf{D} \rangle^{\otimes 2}$ is termed a covariance tensor (Westin et al., 2016).

The approximation (Eq. 5.2.14) is valid for *b*-values up to the convergence radius. If stronger encodings are used, more cumulants are needed to describe the signal accurately (Kiselev and Il'yasov, 2007). In the context of QTI, the cumulant expansion can also be terminated at the sixth cumulant to include a diffusion skewness tensor (Ning et al., 2021). On the other hand, if the encoding strength is weaker, the signal can be expanded only up to the second cumulant as

$$\mathrm{S}(\mathbf{B}) = \mathrm{S}_0 \exp(-\mathbf{B} : \langle \mathbf{D} \rangle). \tag{5.2.15}$$

The signal expression in the Eq. 5.2.14 can be interpreted as the signal model for DKI (5.1.12) and in the Eq. 5.2.15 as the signal model for DTI (Eq. 5.1.8), but where b-tensor **B** is the measurement variable instead of the *b*-value and the encoding direction. However, both DKI and DTI were developed for use with only linear b-tensors ($b_\Delta = 1$).

5.2.2. Powder-averaged Q-space trajectory imaging

It is useful to evaluate parameters that are independent of the orientation of the measured object inside the scanner in order to obtain orientationally-invariant parameters such as MK_A and MK_I. Instead of rotating physically the object and averaging over obtained signal, we can instead rotate the encoding directions. The

signal needs to be averaged across several encoding directions of the b-tensor. This is performed over all b-tensors with the same characteristics except the encoding direction, i.e. over b-tensors with the same *b*-value and b-tensor shape. Other aspects, such as time-dependence of the b-tensor, may also need to be considered, but these are assumed to be negligible in this text. The powder-averaged signal equation analogous to Eq. 5.2.14 is

$$\bar{\mathrm{S}}(\mathbf{B}) = \mathrm{S}_0 \exp\left(-\langle\mathbf{B}\rangle : \langle\mathbf{D}\rangle_{\mathrm{I}} + \frac{1}{2}\langle\mathbf{B}^{\otimes 2}\rangle : \mathbb{C}_{\mathrm{I}}\right), \tag{5.2.16}$$

where two parameters are related to the encoding b-tensor,

$$\langle\mathbf{B}\rangle = b \cdot \frac{1}{3}\mathbf{I}\,, \tag{5.2.17}$$

where $\mathbf{I}$ is the second-order identity tensor, and

$$\langle\mathbf{B}^{\otimes 2}\rangle = b^2 \cdot \left(\mathbb{I}_{\mathrm{bulk}} + \frac{2}{5} b_\Delta^2 \cdot \mathbb{I}_{\mathrm{shear}}\right), \tag{5.2.18}$$

where $\mathbb{I}_{\mathrm{bulk}}$ and $\mathbb{I}_{\mathrm{shear}}$ are two isotropic and orthogonal fourth order tensors, i.e. $\mathbb{I}_{\mathrm{bulk}} : \mathbb{I}_{\mathrm{shear}} = 0$. $\mathbb{I}_{\mathrm{bulk}} = \left(\frac{1}{3}\mathbf{I}\right)^{\otimes 2} = \frac{1}{9}\delta_{ij}\delta_{kl}$ and $\mathbb{I}_{\mathrm{shear}} = \mathbb{I}_{\mathrm{iso}} - \mathbb{I}_{\mathrm{shear}}$ where $\mathbb{I}_{\mathrm{iso}} = \frac{1}{6}\left(\delta_{ik}\delta_{jl} + \delta_{il}\delta_{jk}\right)$ (Westin et al., 2016). Note that the averaging brackets around the b-tensor refers to averaging of all b-tensors with the same shape and b-value. To obtain a powder-averaged signal, the conditions (Eq. 5.2.17 and 5.2.18) need to be satisfied (Paper IV)(Szczepankiewicz et al., 2019a).

Two other parameters of the Eq. 5.2.16 are related to the diffusion,

$$\langle\mathbf{D}\rangle_{\mathrm{I}} = 3\mathrm{MD} \cdot \mathbf{I}, \tag{5.2.19}$$

and

$$\mathbb{C}_{\mathrm{I}} = 9\left(\mathrm{V}_{\mathrm{I}}\mathbb{I}_{\mathrm{bulk}} + \frac{1}{2}\mathrm{V}_{\mu\mathrm{A}}\mathbb{I}_{\mathrm{shear}}\right), \tag{5.2.20}$$

which is termed isotropic covariance tensor, where $\mathrm{V}_{\mu\mathrm{A}}$ is microscopic diffusional variance, $\mathrm{V}_{\mu\mathrm{A}} = \frac{2}{5}\langle\mathrm{V}_\lambda[\mathbf{D}]\rangle$ (Westin et al., 2016).

Finally, using the definition b-tensor shape (Eq. 5.2.4), $\mathrm{MK_I}$ (Eq. 5.2.9) and $\mathrm{MK_A}$ (Eq. 5.2.10) and inserting these into Eq. 5.2.16, the powder-averaged signal can be written as (Szczepankiewicz et al., 2016;Westin et al., 2016),

$$\bar{\mathrm{S}}(b, b_\Delta) = \mathrm{S}_0 \exp\left(-b \cdot \mathrm{MD} + \frac{1}{6} b^2 \cdot \mathrm{MD}^2 \cdot \left(\mathrm{MK_I} + b_\Delta^2 \cdot \mathrm{MK_A}\right)\right). \tag{5.2.21}$$

5.2.3. Estimating MK_A and MK_I

To estimate MK_A and MK_I from the powder-averaged signal, it is useful to rewrite the forward problem (Eq. 5.1.1) from Eq 5.2.21 in a matrix form as (Paper IV)

$$\ln \bar{S}(b, b_\Delta) = \mathbf{e} \cdot \mathbf{p}, \tag{5.2.22}$$

where $\mathbf{e}$ is the vector containing parameters connected to the experiment, $\mathbf{e} = \begin{bmatrix} 1 & -b & b^2/6 & b^2 b_\Delta^2/6 \end{bmatrix}$, and $\mathbf{p}$ is the vector containing parameters connected to the model, $\mathbf{p} = [\ln S_0 \quad \mathrm{MD} \quad \mathrm{MD}^2\,\mathrm{MK_I} \quad \mathrm{MD}^2\,\mathrm{MK_A}]$.

An estimate of the model parameters $\hat{\mathbf{p}}$ can be obtained solving the inverse problem (Eq. 5.1.2) by linear least square fitting,

$$\hat{\mathbf{p}} = \left(\mathbf{E}^{\mathrm{T}} \cdot \mathbf{C} \cdot \mathbf{E}\right)^{-1} \mathbf{E}^{\mathrm{T}} \cdot \mathbf{C} \cdot \ln \bar{\mathbf{S}}, \tag{5.2.23}$$

where $\mathbf{E}^{\mathrm{T}} = \begin{bmatrix} \boldsymbol{e}_1^{\mathrm{T}} & \boldsymbol{e}_2^{\mathrm{T}} & \ldots \boldsymbol{e}_n^{\mathrm{T}} \end{bmatrix}$ is a 4×n matrix containing the encoding protocol with $\boldsymbol{e}_i^{\mathrm{T}}, (i = 1, 2, \ldots n)$ given by a unique combination of b and b_Δ. Furthermore, n corresponds to a number of such combinations or repetitions, $\bar{\mathbf{S}}$ is the signal vector of size n×1, and $\mathbf{C}$ is the n×n diagonal matrix correcting for the heteroscedasticity induced by the logarithm operation (Jones and Cercignani, 2010) and possibly a different number of acquisition directions (m) per shell such that its diagonal elements are given by $\mathbf{C}_{\mathrm{ii}} = \mathbf{S}_{\mathrm{i}}^2 m_{\mathrm{i}}$, where i is the shell index.

5.3. Time-dependent encoding

The spectral frequency formulation of time-dependence allows for the study of which of aspects of the underlying tissue are relevant from a time-dependent perspective and which are encoded into the signal (Stepišnik, 1993). Using this formalism, the signal can be decomposed into two independent quantities from which one describes the encoding, termed the encoding power spectrum $|\mathrm{q}(f)|^2$, and another that describes the effects of structure on the diffusion, termed the diffusion spectrum D(f), which is independent from the encoding (Stepišnik, 1993).

The phase $\phi(\tau)$ at time τ from Eq. 5.1.3 can be expressed as a spin velocity along a q-vector by integrating by parts,

$$\phi(\tau) = \gamma \int_0^\tau \mathrm{g}(t)\mathrm{r}(t)\mathrm{d}t = -\int_0^\tau \mathrm{q}(t)\mathrm{v}(t)\mathrm{d}t, \tag{5.3.1}$$

where $\mathrm{q}(\tau)$ is the q-vector,

$$\mathrm{q}(\tau) = \gamma \int_0^\tau \mathrm{g}(t)\mathrm{d}t. \tag{5.3.2}$$

The signal given by the average over all phase ϕ contributions (Eq. 5.1.4) can be expanded into its cumulants (Kiselev, 2010) as

$$\langle \exp\big(i\phi(\tau)\big)\rangle = \sum_{n=1}^{\infty} \exp(i^n c_n) \tag{5.3.3}$$

where c_1 and c_2 are given by

$$c_1 = \int_0^\tau \mathrm{q}(t)\langle \mathrm{v}(t)\rangle \mathrm{d}t, \tag{5.3.4}$$

$$c_2 = \frac{1}{2}\iint_0^\tau \mathrm{q}(t_1)\mathrm{q}(t_2)\langle \mathrm{v}(t_1)\mathrm{v}(t_2)\rangle \mathrm{d}t_1 \mathrm{d}t_2, \tag{5.3.5}$$

where brackets $\langle\cdot\rangle$ indicate averaging over all spin trajectories and the double integral averages over all times from 0 to τ. In the absence of net spin-flow the first cumulant c_1 is zero. The second cumulant c_2 includes the spin velocity autocorrelation function $\langle \mathrm{v}(t_1)\mathrm{v}(t_2)\rangle$ and the signal is by cumulant expansion up to the second order thus given by

$$\mathrm{S}(\tau) \approx \exp\left(-\frac{1}{2}\iint_0^\tau \mathrm{q}(t_1)\mathrm{q}(t_2)\,\langle \mathrm{v}(t_1)\mathrm{v}(t_2)\rangle\, \mathrm{d}t_1 \mathrm{d}t_2\right). \tag{5.3.6}$$

By assuming that the average of the diffusion process is ergodic, ($\langle \mathrm{v}(t_1)\mathrm{v}(t_2)\rangle = \langle \mathrm{v}(t_1 + t)\mathrm{v}(t_2 + t)\rangle$), the double integral can be reduced to a single dimension. Performing a Fourier transform then yields

$$\mathrm{S}(\tau) \approx \exp\Big(-\int_{-\infty}^{+\infty} \mathrm{D}(f)\cdot|\mathrm{q}(f)|^2\,\mathrm{d}f\Big), \tag{5.3.7}$$

where the signal is separated conveniently into two quantities. The first is termed diffusion spectrum, D(*f*), which is as a Fourier transform of the velocity autocorrelation function,

$$\mathrm{D}(f) = \mathcal{F}\{\langle \mathrm{v}(t_1)\mathrm{v}(t_2)\rangle\} = \frac{1}{2}\int_{-\infty}^{\infty}\langle \mathrm{v}(t_1)\mathrm{v}(\mathrm{t}_2)\rangle \cdot \mathrm{e}^{-2\mathrm{i}\pi\cdot t\cdot f}\,\mathrm{d}t, \tag{5.3.8}$$

where $t = |t_1 - t_2|$, and the second term is the encoding power spectrum, $|\mathrm{q}(f)|^2$, defined from an encoding spectrum q(*f*) as

$$\mathrm{q}(f) = \mathcal{F}\{\mathrm{q}(t)\} = \mathcal{F}\Big\{\gamma\int_0^\tau \mathrm{g}(t)\,\mathrm{d}t\Big\} = \int_{-\infty}^{+\infty}\mathrm{q}(t)\mathrm{e}^{-2\pi\mathrm{i}\cdot t\cdot f}\,\mathrm{d}t, \tag{5.3.9}$$

where *g*(*t*) is the gradient waveform. We can observe that the central equation of the diffusion signal (Eq. 5.3.7) is given by multiplying the diffusion spectrum D(*f*) that

characterizes correlations within the microstructure up to the first order, and the encoding spectrum $|\mathrm{q}(f)|^2$ that dictates which part of the diffusion spectrum that is encoded into the signal. This framework is useful because it enables the separation of the effects of the biological model and studies what features of the model are of relevance for the time-dependent diffusion. It also is instructive in the design of an experiment that optimally encodes these features into the signal.

6. Microstructural features of axons relevant for diffusion MRI

In this chapter, we will investigate which features of the axons are relevant for clinical diffusion MRI experiments from the perspective of time-dependent diffusion MRI. We focus on the intra-axonal space, which can be studied independently from the extra-axonal space because the two spaces are separated by a myelin sheath that can be considered impermeable as it acts as a diffusion barrier at clinically achievable diffusion times (Sen and Basser, 2005). The findings from the study of intra-axonal space can later be incorporated into a broader model of white matter by also considering the extra-axonal space.

The question is which features of axons are relevant for a gross description of their diffusion (Figure 1). By observing the axon microstructure in the transversal plane with respect to the axon propagation, it may seem natural to represent them as cylinders (Figure 1B), which has already been widely considered (Assaf and Basser, 2005;Assaf et al., 2008;Barazany et al., 2009;Alexander et al., 2010). However, by observing axons in the longitudinal plane provides a different intuition. Then may be more natural to represent axons as thin fibers propagating in a non-straight sine-like fashion, referred to as undulations (Figure 1C). The effects of undulations have not so far been widely studied and are considered here (Paper I)(Nilsson et al., 2012;Lee et al., 2020a;Lee et al., 2020b). Furthermore, investigations of the 3D structure of axons (Abdollahzadeh et al., 2019;Lee et al., 2019), features beyond those originating from cylinder-diameter or undulations, might be of relevance (Figure 1D). Example of these may be intra-axon diameter variations (Lee et al., 2020a;Lee et al., 2020b).

This chapter studies the effects of undulations on the diffusion. In particular, parameters of the diffusion spectrum in the perpendicular direction to the propagation of the axons are determined analytically and verified numerically. The undulating thin fiber model and straight cylinder model are compared as competing models of the intra-axonal diffusion and assessed concerning whether the models that assume straight cylinders overestimate the axon diameter in the presence of axonal undulations.

6.1. Diffusion spectrum of straight cylinders

The cylinder diffusion spectrum that characterizes the diffusion perpendicular to the restrictions between planes (1D), cylinders (2D) or a sphere (3D) is given by the infinite sum of Lorentzians (Stepišnik, 1993;Lasič et al., 2009) as

$$\mathrm{D}(f) = \mathrm{D}_0 \sum_{k=1}^{\infty} \frac{\mathrm{a}_k \mathrm{B}_k f^2}{\mathrm{a}_k^2 \mathrm{D}_0^2 + f^2}, \tag{6.1.1}$$

where a_k and B_k are coefficients depending on the geometry given by

$$\mathrm{a}_k = \left(\frac{\zeta_k}{\mathrm{R}}\right)^2, \tag{6.1.2}$$

$$\mathrm{B}_k = \frac{2(\mathrm{R}/\zeta_k)}{\zeta_k^2 + 1 - \mathrm{d}}. \tag{6.1.3}$$

ζ_k are the kernels of

$$\zeta \mathrm{J}_{\mathrm{d}/2-1}(\zeta) - (d-1)\mathrm{J}_{\mathrm{d}/2}(\zeta), \tag{6.1.4}$$

where $\mathrm{J}_\nu(\zeta)$ is the ν-th order Bessel function, d = 1,2, or 3 for planar, cylindrical or spherical restrictions and 2R is the diameter of the restrictions. Eq. 6.1.1 describes analytically the aspects of the time-dependent diffusion of straight-cylinders characterized by diameter d.

6.2. Effects of undulating thin fibers

To study the effects of undulations, we need to isolate them from other features of axons and represent them by a model that captures their primary structure but also disregards their unimportant details (Nilsson et al., 2012). We proposed an undulating thin-fiber model as a toy-model of undulations (Figure 6A), inspired by histology images (Figure 1C). Three different cases of the model with an increasing degree of complexity were studied: first, thin fibers propagating like sine waves with a single set of amplitude and wavelength, referred to as 1-harmonic case; second, which combines multiple sine wave fibers characterized by a distribution of amplitudes and wavelengths, referred to as the *n*-harmonic case; and third, the effect of disorder is considered by adding a noise to the phase of the sine wave, referred to as the stochastic case.

The question is how to represent the diffusion spectrum perpendicular to the propagation of axons. Numerical simulations showed that diffusion spectra arising from undulating thin-fibers as well as from straight-cylinders can be approximated by a single Lorentzian term (Figure 6B),

$$\mathrm{D}(f) \approx D_{\mathrm{hi}} \frac{f^2}{f_\Delta^2 + f^2}. \tag{6.2.1}$$

This parameterization is useful because it means that only two free parameters need to be analyzed: D_{hi}, which a parameter that describes the height of the spectrum at high frequencies and f_Δ, the frequency of half-width half maximum, i.e., when $\mathrm{D}(f_\Delta) = D_{\mathrm{hi}}/2$. The infinite sum of Lorentzian that analytically predicts the diffusion spectra arising from straight-cylinders (Eq. 6.1.1) can also be approximated by the single Lorentzian term (Eq. 6.2.1).

The question arises how features of the undulating fibers maps onto the spectral width f_Δ and the spectral height D_{hi}. Here it is useful to consider what we refer to as the microscopic orientation dispersion (μOD). It is a measure of dispersion within fibers, and defined as

$$\mu\mathrm{OD} = \langle \sin^2\big(\theta(x)\big) \rangle, \tag{6.2.2}$$

where x is the position of the segment, $\langle \cdot \rangle$ denotes averaging over all fiber segments, and θ is the angle between the direction of the fiber segment and the main fiber direction. In the 1-harmonic and stochastic case, the f_Δ and spectral height D_{hi} can be predicted as

$$D_{\mathrm{hi}} = D_0 \cdot \mu\mathrm{OD}, \tag{6.2.3}$$

$$f_\Delta \approx \mathrm{k_h} \cdot \frac{\mathrm{D_0}}{\mathrm{a^2}} \cdot \mu\mathrm{OD}, \tag{6.2.4}$$

where $\mathrm{k_h}$ is a proportionality constant. In the n-harmonic case the Eqs. 6.2.3 and 6.2.4 need to be modified to consider average orientation dispersion and weighting by μOD,

$$D_{\mathrm{hi}} = D_0 \cdot \langle \mu\mathrm{OD}_i \rangle, \tag{6.2.5}$$

$$f_\Delta \approx \mathrm{k_s} \cdot \mathrm{D_0} \frac{\langle \mu\mathrm{OD}_i^2 / a_i^2 \rangle}{\langle \mu\mathrm{OD_i} \rangle}, \tag{6.2.6}$$

where $\mathrm{k_s}$ is a proportionality constant. These predictions were verified by numerical simulations (Figure 6C). Note that the diffusion spectrum is uniquely given by Eqs. 6.2.3-6.2.6, but that does not apply in the opposite direction because a vast number of undulating thin-fibers, which may be any of the 3 cases, map onto a single

diffusion spectrum. It follows that it is also not possible to use dMRI to map all the features of undulating thin-fibers. At best, at least in principle, its amplitude and μOD can be estimated from dMRI data.

6.3. Implications for axon diameter mapping

By comparing diffusion spectra of undulating fibers with undulating cylinders we found that at low diameters the properties of the diffusion spectrum are mainly determined by features of the undulations (the microscopic orientation dispersion and the undulation amplitude), whereas at larger diameters, the properties are mainly determined by the cylinder diameter (Figure 6D). We found that undulating thin fibers have a diffusion time dependence that is similar to that of cylinders, at least for lower frequencies (longer diffusion times). This can lead to overestimated axon diameters when interpreting data from undulating thin axons using models that represent axons by straight cylinders. When diffusion-weighted signals are simulated using the encoding protocol by Alexander et al. (2010) in an undulation model, yet analyzed with a model assuming straight cylinders, the cylinder diameter is overestimated by an amount determined by the undulation amplitude (Paper I). Observed effects of time-dependent diffusion in brain white matter may be attributed to undulation parameters rather than the axon diameter.

Similar considerations were proposed based on numerical simulations in segmented axons from 3D electron microscopy images of white matter (visualized in Figure 1C) (Abdollahzadeh et al., 2019;Lee et al., 2019). (Lee et al., 2020a;Lee et al., 2020b) found that the estimate of the axon diameter is confounded by undulations as well as diameter variations within individual axons. The effects of undulations were found to be most prominent at low *b*-values, and therefore effects of undulations can be considerably reduced by using higher *b*-values where the estimated diameter is mostly given by a combination of the axon caliber (dominated by the thickest axons) and axon diameter variations.

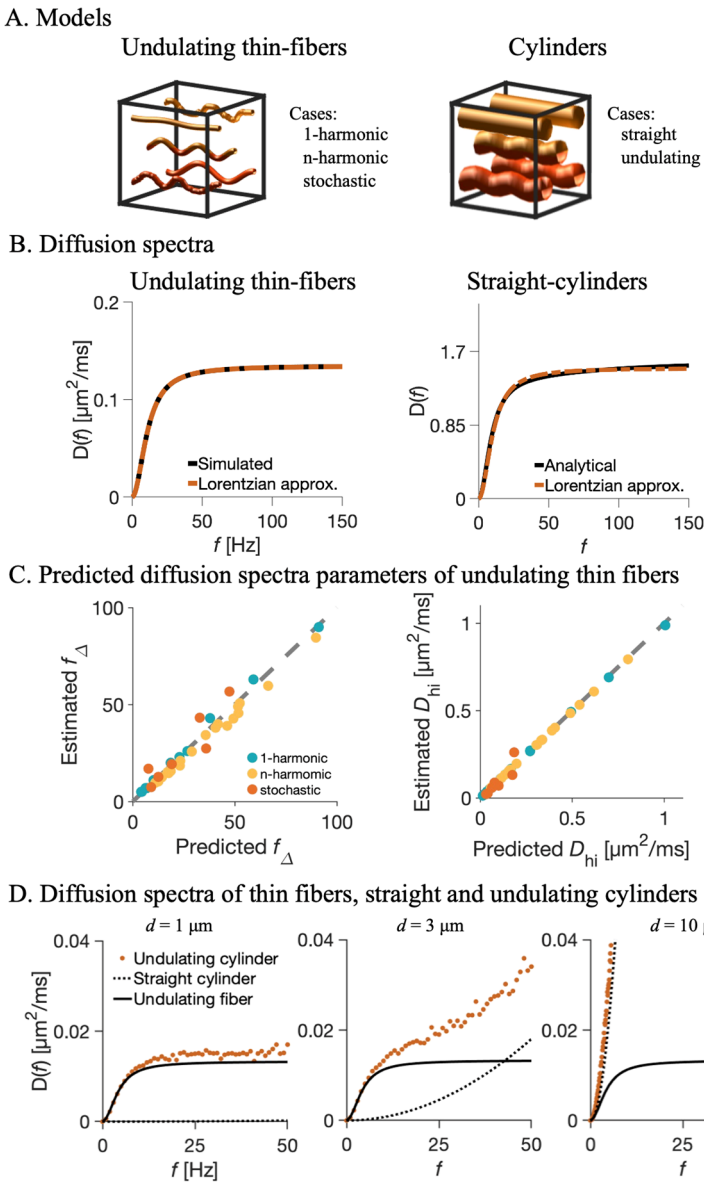

Figure 6. Time-dependent characteristics of undulating thin fiber and cylinder models. Panel A shows three cases of the undulating thin fiber model (1-harmonic, *n*-harmonic and stochastic) as well as two cases of the cylinder model (straight and undulating). The 1-harmonic case are sine waves with a single amplitude and wavelength, *n*-harmonic has a distribution of amplitudes and wavelengths and the stochastic has a stochastic phase. Panel B shows that the 1-harmonic case of undulating thin-fiber and straight-cylinders are well approximated by a single Lorentzian term. Both *n*-harmonic and stochastic cases are also well approximated by a single Lorentzian (Paper I). Panel C shows that diffusion spectra parameters can be predicted by the properties of the undulating thin fiber model in all three cases. Finally, panel D shows that for low diameters the diffusion spectra of the undulating cylinders are virtually due to its undulation because the spectra coincide with the 1-harmonic case of undulating thin fibers. On the other hand, at high cylinder diameters the spectral features are mainly determined by the cylinder diameter. Figure adapted from Paper I, published by Wiley and licensed under CC BY 4.0.

6.4. Conclusions

In Paper I, we presented a toy-model of axonal undulations—a sine wave—which we used to study the diffusion perpendicular to the direction of propagation of the axons. We showed that two distinct axonal features—undulations and restriction at biologically relevant undulation parameters and axonal diameters—have virtually identical diffusional characteristics at intermediate to long diffusion times. This means that they are experimentally indistinguishable in this regime. Axonal undulations can therefore bias diameter estimation strategies if straight cylinders are used to model the intra-axonal diffusion. Diffusion encoding with encoding power at frequencies higher than those enabled by pulsed gradient schemes may help to disentangle effects of undulations and sizes.

7. Contrasts by tensor-valued encoding

Tensor-valued encoding yields an experimental variable, termed b-tensor shape, b_Δ, and this chapter provides an overview of the effects of varying the b-tensor shape without modelling to "see what is in the signal." To retain clarity, the simplest case—diffusion-weighted images at low and high *b*-values obtained with spherical b-tensor encoding (referred to as STE-DWI, $b_\Delta = 0$)—is investigated (Westin et al., 2016). This is compared to the conventional DWI obtained with a linear b-tensor that is averaged across several directions (LTE-DWI, $b_\Delta = 1$) (Stejskal and Tanner, 1965).

7.1. Contrasts mechanism of STE-DWI

STE-DWI provides a contrast complementary to LTE-DWI at higher *b*-values. At lower *b*-values both LTE and STE encode for average diffusivity because the contribution of higher order terms in the signal equation (Eq. 5.2.14) are negligible. This means at lower *b*-values the signal equation becomes essentially the one from DTI (Eq. 5.2.15) where MD is the sole parameter. On the other hand, at higher *b*-values the contribution from higher order terms is not negligible (Eq. 5.2.14, Eq. 5.2.21). The Eq. 5.2.21 shows that LTE encodes for average diffusivity and a combination of diffusion anisotropy and isotropic heterogeneity, whereas STE encodes only for average diffusivity and isotropic heterogeneity (Szczepankiewicz et al., 2016;Westin et al., 2016). This is because at higher *b*-values, in the case of STE ($b_\Delta = 0$), MD and MK_I contributes to the signal but the contribution from MK_A is zero (Eq. 5.2.21). On the other hand, in the case LTE ($b_\Delta = 1$) all three parameters contribute to the signal.

The power of tensor-valued encoding lies in its ability to separate the presence of diffusion anisotropy with orientation dispersion from isotropic heterogeneity. For example, consider white matter tracts that have high MK_A due the anisotropy and orientation dispersion of the axons (Beaulieu, 2002;Jeurissen et al., 2013). The MK_I, on the other hand, is low to intermediate (Paper III; Paper IV)(Szczepankiewicz et al., 2015). Therefore, STE and LTE are different at higher *b*-values (from

approximately 1400 s/mm^2 and above). STE attenuates the white matter signal more than LTE does (orange arrows in Figure 7A)(Paper III), as the contribution to the signal from MK_A vanishes with STE.

7.2. STE-DWI increases conspicuity in gliomas

STE-DWI can be used at higher b-values (b = 2000 s/mm^2) to increase the conspicuity of tumor-related hyperintensities by suppressing the white matter signal (Paper III). The underlying mechanism is that white matter is predominately composed of elongated and orientationally dispersed axons (Jeurissen et al., 2013), which means we expect that they yield high diffusion anisotropy (Beaulieu, 2002). Glioma tumor tissue is, on the other hand, composed of predominately tightly packed, small, and tightly packed approximately spherical cells which means that we can expect them to yield low diffusivity with low diffusion anisotropy (Szczepankiewicz et al., 2015;Szczepankiewicz et al., 2016). Therefore, we expect STE-DWI to suppress the signal in white matter but not in regions with dense tumor cells.

To test whether glioma hyperintensities are more conspicuous to white matter with STE-DWI rather than LTE-DWI, we investigated 25 patients diagnosed with glioma tumors (Paper III). We compared the signal-intensity ratio of glioma hyperintensities and normally appearing contralateral white matter (NAWM), which is defined as

$$\mathrm{SIR}(X) = \frac{\langle \mathrm{S}_{\mathrm{hyperintensity}}(X) \rangle}{\langle \mathrm{S}_{\mathrm{NAWM}}(X) \rangle}, \tag{7.2.1}$$

where X is a signal either obtained from STE-DWI at b-value 2000 s/mm^2 or from LTE-DWI at the same b-value, and $\langle \cdot \rangle$ represents the mean value across region-of-interest (ROI).

We found that the SIR increased in all (100 %) cases and was significantly higher for STE-DWI than LTE-DWI, with a median (interquartile range) of 1.9 (1.6 – 2.1) vs. 1.4 (1.3 – 1.7) ($p < 10^{-4}$; paired Wilcoxon signed-rank test; Figure 7B) (Paper III). With STE-DWI, the SIR increased on average by 28 %. Moreover, in 10 of the 25 patients (40 %) that had a hyperintensity unrelated to white matter, the SIR for STE-DWI was above 2, but with LTE-DWI, the SIR was below 2 for all patients.

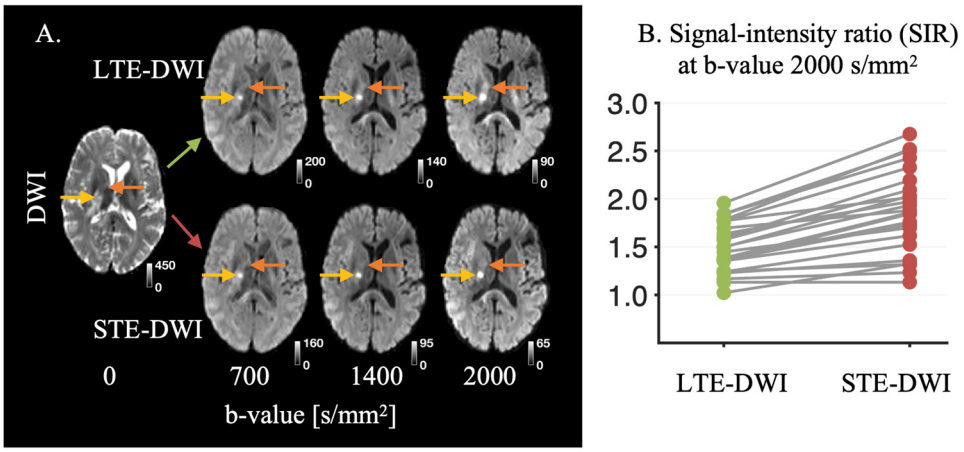

Figure 7. Contrast mechanism of STE and increased conspicuity in gliomas. Panel A shows that at higher *b*-values STE attenuates white matter more than LTE compared. Orange arrows: corticospinal tract, yellow arrows: glioma tumor-related hyperintensity. Panel B shows that the signal-intensity-ratios (SIR) obtained by conventional encoding (LTE-DWI) and spherical tensor encoding (STE-DWI) at a *b*-value of 2000 s/mm^2. In all (100 %) cases, the SIRs from STE-DWI were higher than those obtained by LTE-DWI (median ± standard deviation; SIR 1.46 ± 0.24 vs 1.91 ± 0.40; paired Wilcoxon signed-rank test, $p < 10^{-4}$). Figure adapted from Paper III, published by Frontiers Media licensed under CC BY 4.0.

STE-DWI could thus help to improve diagnostic confidence on the individual patient level. Figure 8 shows images of a glioblastoma patient compared with images from a patient without a brain tumor-related MRI abnormality. Here, several LTE-DWI and STE-DWI hyperintensities can be observed. Some hyperintensities are found on both LTE- and STE-DWI and may be due to a T2 shine-through effect (blue arrows). Some hyperintensities that are related to white matter are suppressed with STE-DWI but not by LTE-DWI (orange arrows). Importantly, some STE-DWI hyperintensities (green arrows) may be otherwise "hidden" with LTE-DWI under these white matter-related hyperintensities. These hyperintensities that coincide are in the example surrounded by Gd-enhancements (green arrows in the panel A). Thereby, STE-DWI amplifies the contrast from non-white-matter tissue.

The results show that STE-DWI could be used to visualize tumor-related hyperintensities infiltrating or disrupting the white matter tracts (Figure 8B). This is important, as the tracts are a route of spreading for glioma tumor cells (Giese et al., 1996;Giovanna and Kaye, 2007). STE-DWI could also improve hyperintensity delineation and detection because, unlike with LTE-DWI, a confounding factor (white matter) is suppressed. That is because STE-DWI at higher *b*-values ($b = 2000$ s/mm^2) attenuates anisotropic tissue components and emphasizes isotropic low-diffusion components contributing to the diffusion-weighed signal at higher *b*-values. STE-DWI emphasizes tissues, such as dense glioma tumors, with spherical and tightly packed cells that exhibit low diffusivity in all directions.

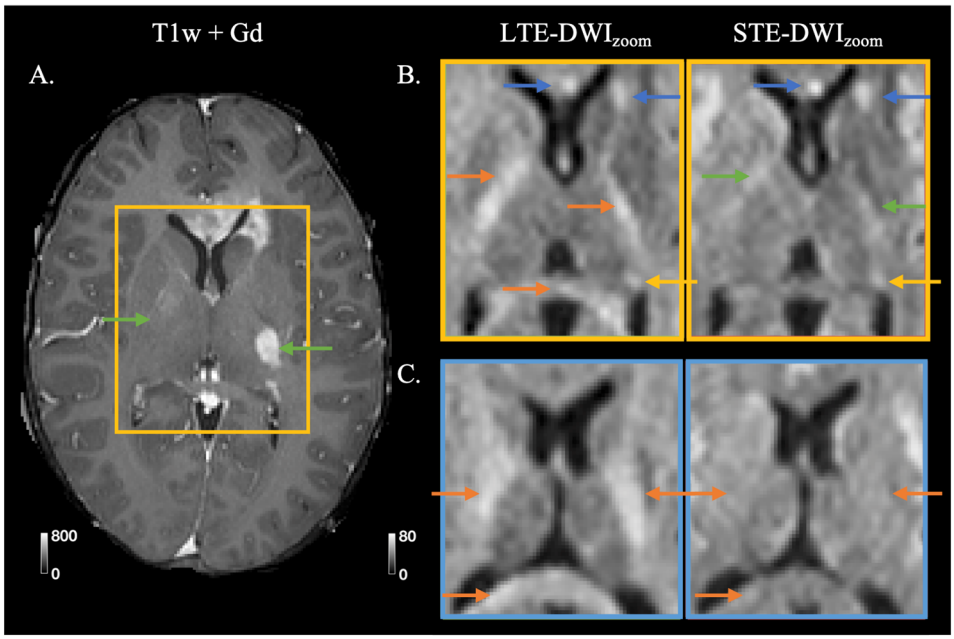

Figure 8. Suppression of white-matter-related hyperintensities by STE-DWI could improve diagnostic confidence. Figure shows a 31-year-old male diagnosed with glioblastoma grade IV. Panel A shows a T1w + Gd image of a patient with glioblastoma grade IV. Green arrows: Gd-enhancing lesions. Panel B shows a zoom-in on LTE- and STE-DWI in the patient (yellow borders). STE-DWI suppresses hyperintensities related to white matter (orange arrows) and thereby makes more apparent those that are unrelated to white matter (blue, yellow and green arrows). Panel C illustrates that in a subject without relevant MRI abnormalities all white-matter-related hyperintensities seen with LTE-DWI disappear with STE-DWI (orange arrows). Figure adapted from Paper III, published by Frontiers Media and licensed under CC BY 4.0.

7.3. STE-DWI for dot fraction imaging

STE-DWI at even higher *b*-values (*b* over 4000 s/mm^2) can be used to serve as a marker for small and isotropically restricted water compartments, often referred as the dot fraction (Lundell et al., 2019;Tax et al., 2020). These can arise from e.g. spherical cell bodies, where the diffusion is restricted in all directions. In such conditions, the diffusion signal is non-zero and nearly non-decaying at high enough *b*-values and, thereby, the ADC is near-zero.

In cerebellar gray matter, a signal signature of a dot fraction has been found using STE-DWI (Vis et al., 2021). Figure 9 shows a coronal slice of a healthy volunteer. Panel A shows a T1w image and panel B STE-DWI at b = 4000 s/mm^2. Panel C shows a Nissl-stained histology image (not same subject) that visualizes genetic material.

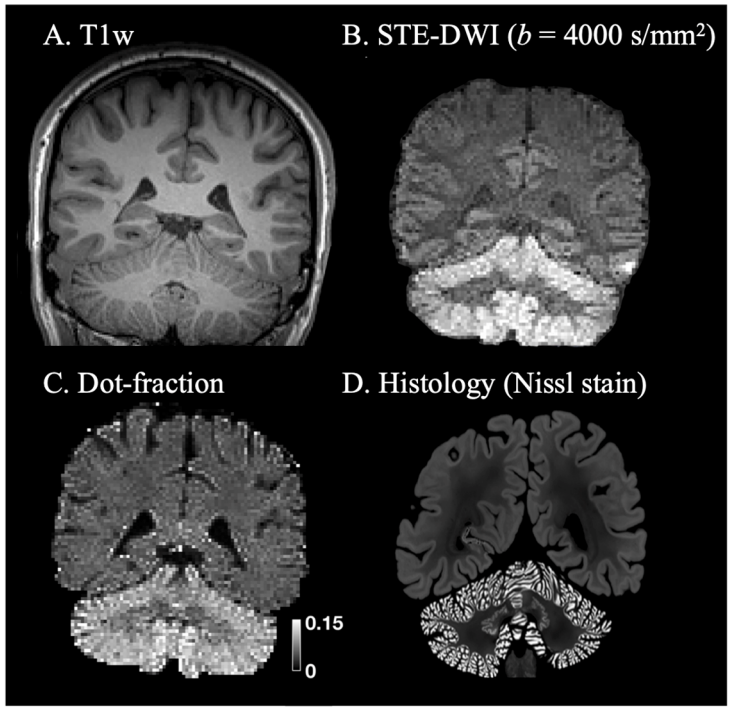

Figure 9. STE-DWI at high *b*-values for a dot fraction specific contrast. Panel A shows a coronal slice of T1w image of a healthy volunteer. Panel B shows the same anatomical location where STE-DWI at b = 4000 s/mm^2 emphasizes gray matter in cerebellum. Panel C shows estimated dot-fraction. Panel D shows a similar anatomical location of a Nissl-stained histology. Figure adapted from (Vis et al., 2021), published by Elsevier and licensed under CC BY 4.0.

STE-DWI is more suitable than LTE-DWI to identify the dot fractions because at high *b*-values it has a high signal only where the isotropic diffusion is low, whereas with LTE-DWI a high signal could be attributed to either low isotropic diffusion or high diffusion anisotropy and measurements not perfectly aligned with all fibers in the voxel (Szczepankiewicz et al., 2015).

7.4. Conclusions

STE-DWI at higher *b*-values can be used to increase the conspicuity of glioma-tumor-related hyperintensities relative to white matter. It can also be used as an imaging marker for small isotropic spaces, referred to as dot fraction imaging. This is because the STE-DWI signal at higher *b*-values is high only where there are microenvironments with low diffusivity in all directions.

8. Q-space trajectory imaging of intracranial tumors

In this chapter, the application of Q-space trajectory imaging (QTI) to intracranial tumors is examined. The discussion builds on the previously introduced coupling between tensor-valued encoding and the diffusion tensor distribution (DTD) for separating MK into its components—MK_A and MK_I—where MK is the sum of the two (Chapters 5.2.1, 5.2.2 and 5.2.3). This approach is here referred to as QTI. The analysis can also be performed by considering μFA (Eq. 5.2.13) instead and the results of studies based on μFA will be briefly reviewed.

QTI may be beneficial for studies of intracranial tumors for several reasons. First, considering only DWI (Chapter 7) yields non-specific signal values, which need to be interpreted based on experience rather than conceptual knowledge. This limitation is the same for STE-DWI as for conventional LTE-DWI, although some extra knowledge can be obtained by comparing the two as discussed in the previous chapter. Second, the DTD, which is an essential part of QTI, is suitable for modelling of multi-gaussian diffusion. This is appealing for capturing cancer heterogeneity because within an image voxel there may be many intra-voxel compartments characterized by distinct anisotropies or apparent diffusivities. Third, initial applications of QTI showed that distinct values of MK_A and MK_I were associated with glioma and meningioma tumors but both tumor types yielded similar MK values (Paper IV)(Szczepankiewicz et al., 2016).

QTI has already been applied in several conditions affecting the human brain. In epilepsy, MK_A offered a more robust differentiation of cortex and white matter in the presurgical evaluation of malformations of cortical development (Lampinen et al., 2020b). In multiple sclerosis, μFA showed a significant association with physical disability, cognitive dysfunction and lesion load in specific tract systems when FA did not (Andersen et al., 2020). In schizophrenia, an increase in the variance of isotropic diffusivity was observed (Westin et al., 2016). QTI has also been applied to healthy brain microstructure to facilitate model parameter estimation (Szczepankiewicz et al., 2015;Dhital et al., 2018;Lampinen et al., 2019;Szczepankiewicz et al., 2019a;Afzali et al., 2020;Afzali et al., 2021;de Almeida Martins et al., 2021;Reymbaut et al., 2021).

This chapter reviews results obtained when QTI is adapted and applied for brain tumors imaging. First, the QTI imaging protocol is adjusted for intracranial tumors imaging where the focus is on fast execution of the protocol and on estimating the range of MK_A and MK_I values for distinct tumors (Paper IV). We also investigated whether MK_A and MK_I can answer some of the pressing clinical questions in a more detailed study of meningioma tumors (Paper V). We will thus compare what can be achieved with conventional parameters—FA from DTI and MK from DKI.

8.1. QTI is feasible in intracranial tumors

To minimize the scan time of a QTI protocol for intracranial tumors, we designed a protocol that can provide estimates of QTI parameters with a minimal number of measurements. We refer to this protocol as the minimal one, and it achieved a scan time of 3 minutes. We compared the minimal protocol to a protocol that we refer to as the full one, which had scan time of 5 minutes.

In the design of the minimal protocol, three aspects need to be considered: matrix inversion (Eq. 5.2.2) and powder-averaging of the signal at low (Eq. 5.2.17) and high *b*-values (Eq. 5.2.18). Firstly, at least 4 independent measurement shells are needed to invert the matrix (Eq. 5.2.2) to estimate 4 parameters (S_0, MD, MK_A and MK_I, Eq. 5.2.21). Secondly, the powder averaging needs a sufficient number of directions so that orientational variance is minimized. A reduced number of directions can be used in tumor imaging because the voxel-level anisotropy of intracranial tumors is relatively low (FA < 0.5) (Szczepankiewicz et al., 2019a). To find out the number of rotations needed for the signal to be sufficiently rotationally-invariant we can calculate the coefficient of variation (CV) across b-tensor rotations for a signal simulated with a given FA and b-value, and consider the signal to be sufficiently rotationally invariant when its coefficient of variation (CV) is less than 1 % (Szczepankiewicz et al., 2019a). The results showed that at higher *b*-values of 2000 s/mm^2 it is sufficient to use only six directions from the icosahedral scheme to obtain powder-averaged signal (Eq. 5.2.18) when the FA is below 0.5.

The minimal protocol featured 9 measurements: 3 STE at *b*-values 0, 1000 and 2000 s/mm^2 and only 6 rotations of LTE at *b*-value 2000 s/mm^2 because FA is below 0.5 for most intracranial tumors (Szczepankiewicz et al., 2019a). We found that the minimal protocol provides estimates of MD, MK_A and MK_I with similar parameter values and similar errors as the full protocol (Figure 10).

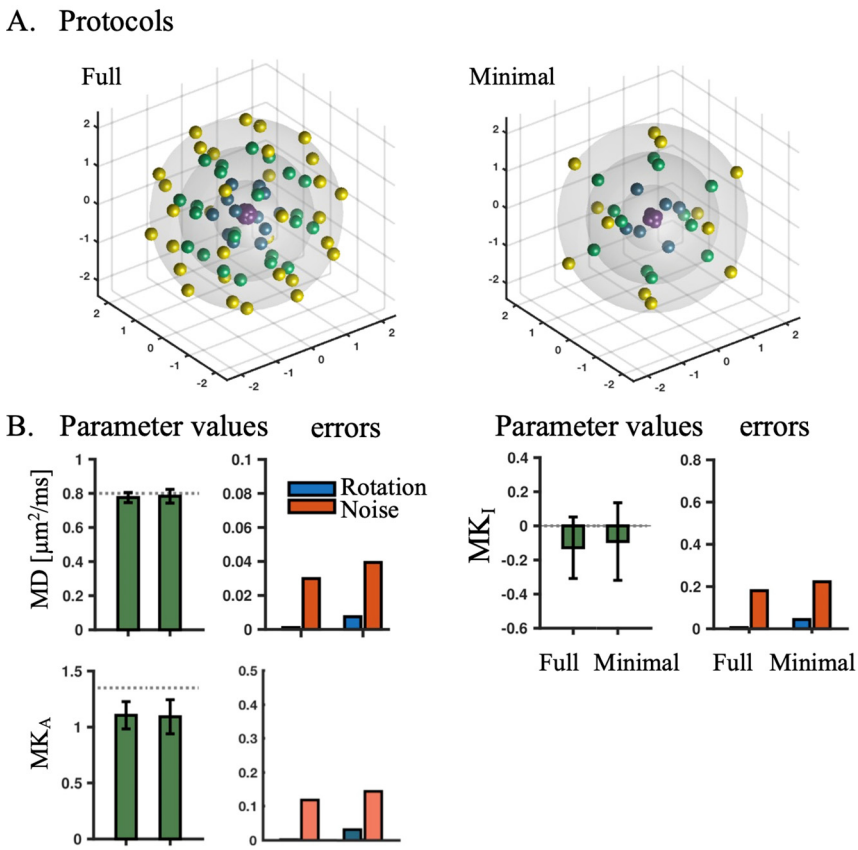

Figure 10. Numerical simulations of accuracy and precision for the minimal protocol. Panel A shows the dMRI acquisition using the linear b-tensors. Panel B shows on the left side values of MD, MK_A and MK_I (error bars show standard deviation and dashed lines true values). On the right side are shown errors originating from rotation variance and noise. Figure adapted from Paper IV, published by Wiley and licensed under CC BY-NC 4.0.

We found that the estimation of MK_A and MK_I is feasible in clinically relevant scan times and unbiased when compared to the full protocol (Paper IV). A wide range of MK_A and MK_I values was found across different types of intracranial tumors (Paper IV). Glioblastomas had a lower average MK_A than meningiomas (MK_A = 0.29 ± 0.06 vs. 0.45 ± 0.08, p = 0.003, U-test), and metastases had higher MK_I (MK_I = 0.57 ± 0.07) than both the glioblastomas (0.44 ± 0.06 p < 0.001, U-test) and meningiomas (0.46 ± 0.06, p = 0.03, U-test). The glioma category included a diverse set of gliomas, and they showed high variability. When compared with normal-appearing white matter, all tumors except for two had lower MK_A, higher MK_I, and lower MK. In Figure 11, we showcase MD, MK_A and MK_I in 4 different tumor types.

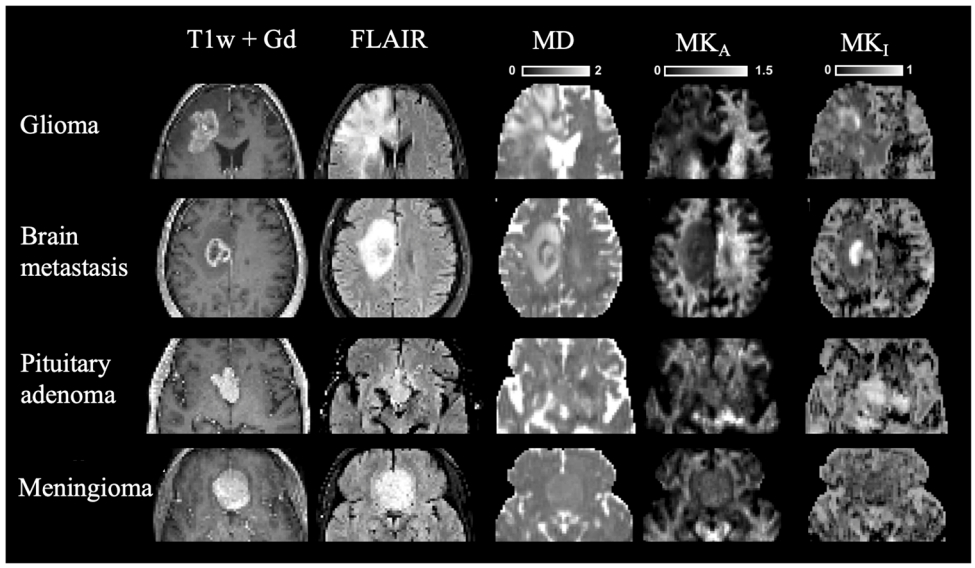

Figure 11. MRI parameter maps in different intracranial tumor types. Both the glioblastoma and brain metastasis cases exhibited low MK_A, whereas the pituitary adenoma and the meningioma cases exhibited higher MK_A. All tumors in this figure, except the meningioma, displayed regions with markedly elevated MK_I. Figure adapted from Paper IV, published by Wiley and licensed under CC BY-NC 4.0.

8.2. QTI for presurgical meningioma evaluation

We applied QTI to meningioma tumors in an exploratory study and aimed at investigating whether MK_A and MK_I in comparison with MK from DKI and FA from DTI can add to the preoperative prediction of meningioma consistency, grade and type (Paper V). We investigated these parameters in two different ROIs – in the ROI encompassing the whole tumor (referred to as whole-tumor ROI) and in the surrounding tissue outside of tumor region, which is maximally 2 voxels wide, to capture the effects of the tumor on the surrounding tissue (referred to as rim-ROI). The whole-tumor ROI was defined based on the contrast-enhanced T1w + Gd images to include the maximum extent of the tumor. The rim-ROI was defined just outside of the enhancement.

As for meningioma consistency, we found that the lower 10^{th} percentiles of MK and MK_A in the whole-tumor were associated with firm consistency compared with pooled soft and variable consistency (n = 7 vs 9; U-test, p = 0.02 for $MK_{A\,10}$ and p = 0.04 for MK_{10}) and the lower 10^{th} percentile of MD with variable against soft and firm (n = 5 vs 11; U-test, p = 0.02). Therefore, the firm consistency is associated with the presence of voxels that have lower MK as well as MK_A.

As for meningioma grade, a higher standard deviation of MK_I in the rim was associated with lower grade (n = 22 vs 8; U test, p = 0.04) and in the MK_I maps we observed an elevated rim-like structure that could be associated with grade.

As for meningioma type, higher median MK_A and lower median MK_I was associated with psammomatous type from other pooled meningioma types (n = 5 vs 25; p = 0.03 for MK_A and p = 0.03 and p = 0.04 for MK_I; U-test).

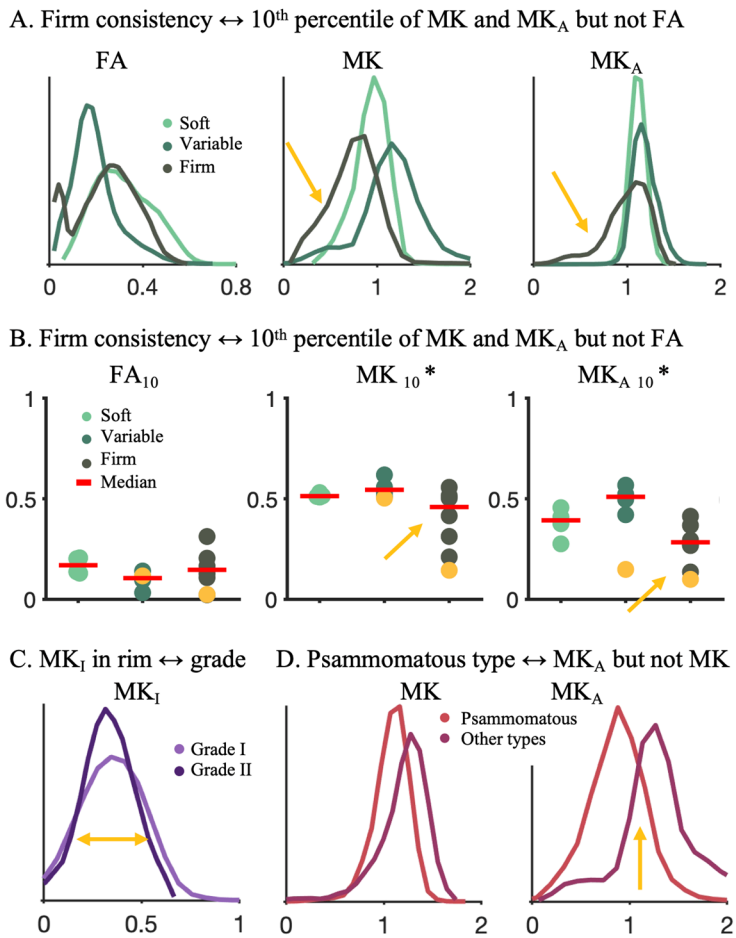

Figure 12. Association with consistency, grade and type with FA, MK, MK_A and MK_I parameters. Panel A shows pooled distributions of parameter-values of FA, MK and MK_A in the whole-tumor ROI among soft, variable, and firm meningioma consistency. The histograms suggests that percentiles or the standard deviation (yellow arrows) could be useful for differentiating the consistency. Panel B shows that the firm consistency is significantly different from the pooled soft or variable consistency tumors based on the 10th percentile within the whole-tumor ROI of MK_{10} and $MK_{A\,10}$ but not FA_{10} (p = 0.04 for MK_{10} and p = 0.02 for $MK_{A\,10}$; U-test). Panel C shows the MK_I distribution in grade I and II meningiomas within the rim ROI. The standard deviation within the rim ROI of MK_I of grade I was significantly higher than that of grade II meningioma (n = 22 vs 8; p = 0.04; U-test). Finally, panel D shows distributions of MK and MK_A in psammomatous and other meningioma types in the whole-tumor ROI. The psammomatous type is significantly different from the others in median of MK_A but not in MK (n = 5 vs 24; p = 0.03; U-test). Significant parameters marked with an asterisk (*), or yellow arrows. Figure adapted from Paper V, published by Elsevier and licensed under CC BY 4.0.

Considering MK_A and MK_I instead of MK could be useful for separating several intracranial tumor types because different values of MK_A and MK_I are associated with gliomas, metastases or meningiomas but MK may be similar (Paper IV)(Szczepankiewicz et al., 2016). For example, the majority of MK in meningiomas originates from a high MK_A component because MK_I in meningiomas is low (Szczepankiewicz et al., 2016), which also explains why not only MK_A but also MK is associated with firm consistency (Figure 12A and 12B).

Considering MK_I and MK_A rather than MK is also of relevance in meningioma grading and typing. The MK_I in the rim was the only parameter to be associated with meningioma grade (Figure 12C) (Paper V), and MK_A was associated with psammomatous type but not MK (Figure 12D). In all of the associations, however, an important limitation is the low statistical power (below 80 %) because of the limited number of patients included in the cohort.

8.3. QTI in glioma tumors

Other studies have also applied QTI to study intracranial tumors (Afzali et al., 2022). (Li et al., 2021) studied whether QTI could be associated with glioma grade or molecular classification. On a group level, most metrics (FA, MK_A, MK_I, MK, μFA) were significantly higher in high-grade than in low-grade gliomas (FA: $p = 0.047$; others $p < 0.001$)., while MD was significantly lower (MD: $p = 0.037$). All metrics distinguished IDH wild-type from IDH mutation (MK_I: $p = 0.003$; others: $p < 0.001$). The metrics that were the most strongly associated with high-grade and low-grade and wild-type and mutated IDH tumors were MK and FA respectively (AUC 0.866 and 0.881). All diffusion metrics except FA showed significant correlation with the Ki-67 labeling index, which is a cellular marker of proliferation and a prognostic marker in meningiomas (Liu et al., 2020), where MK_I had the highest correlation coefficient ($r = 0.618$). Furthermore, Szczepankiewicz et al. (2020) related QTI to grade, tumor recurrence and presence of enhancements on post-gadolinium T1w maps. Average MK_I was reported to be significantly associated with the grades. MK was the strongest predictor of the presence of enhancements on T1w scans and both MK and MK_I predicted tumor recurrence.

8.4. Conclusions

We found that QTI is feasible in intracranial cancer imaging and provides a complementary contrast. Its clinical utility remains to be tested and for this larger cohorts are needed.

- In Paper IV, we evaluated the feasibility of a QTI protocol with a 3-minute-long scan time for assessment of MK_A and MK_I in patients with intracranial tumors. We found that evaluation of the MK_A and MK_I in intracranial tumor patients is feasible in clinically relevant scan times in a wide range of tumors.
- In Paper V, we investigated whether tensor-valued diffusion MRI can add to the preoperative prediction of meningioma consistency, grade and type and found that parameters from tensor-valued dMRI are associated with consistency, grade and type.

9. Microstructural features of intracranial tumors relevant to diffusion MRI

The central question in cancer modelling is what microstructural features of the tissue that influence the diffusion process. The number of potential candidates for microstructural features is vast because cancer microstructure is heterogeneous on several levels. It is diverse among tumor types in different organs. It is also diverse across tumor subtypes, for example, it differs substantially among meningioma tumor subtypes as visualized in the Figure 13A. The microstructure is also different with respect to a tumor mass among different image voxels but also within a single one, where it can contain different types of components, such as microvasculature, densely packed cells, fibrotic tissue, psammoma bodies, collagen fiber, microcysts, scarring or necrosis (Nilsson et al., 2018). These components have a different imprint on the diffusion process and therefore on the dMRI parameters.

The problem is that we do not know what microstructural features of cancer are relevant for the dMRI parameters. Current interpretations tend to rely on singular features such as cell density for the explanation of MD (Eq. 5.1.10) or tissue anisotropy for FA (Eq. 5.1.11). As the true cell density and tissue anisotropy is not known, we need to use proxies for these. Often cell nuclei count density from histology is used as a proxy for cell density (CD) and image anisotropy (IA) obtained from structure tensor analysis of histology images (Bigun, 1987;Budde and Frank, 2012) as a proxy for tissue anisotropy. Using such proxies, MD has been found to be inversely proportional to cell density in different types of tumors (Chen et al., 2013) but also within glioma tumors (LaViolette et al., 2014). This means that MD is often used to identify viable tumor regions with high CD.

The problem is that MD is also affected by tissue properties other than CD, including cell size (Szafer et al., 1995), nuclear sizes (Xu et al., 2009), membrane permeability (Colvin et al., 2011) and the presence of collagen (Egnell et al., 2020) or necrosis (Patterson et al., 2008). Moreover, the inverse relation with CD is not always found and the role of the tumor stroma is highlighted (Squillaci et al., 2004;Yoshikawa et al., 2008). Furthermore, FA has been interpreted as reflecting tissue anisotropy, that is, the presence of elongated cellular structures. The problem is that fractional anisotropy is a measure of voxel-level averaged anisotropy. Tissue

composed of elongated cells with high orientation dispersion would yield low FA just as one composed of isotropic cells (Szczepankiewicz et al., 2015).

This chapter focuses on the interpretation of dMRI parameters in terms of tumor microstructure. The central question is to what degree cell density and image anisotropy are associated with MD and in-plane fractional anisotropy (FA_{IP}), respectively, from DTI measurements. The in-plane fractional anisotropy is analogous to the common FA, but it disregards diffusion in the out-of-plane direction so that it can be more straightforwardly compared to the anisotropy observed in thin histological slices. To test this, high-resolution dMRI and microscopy was performed on the same samples to test whether features from the microscopy images can predict local variations of MD and FA_{IP}.

9.1. Study design

A total of 16 meningioma tumor samples were obtained after neurosurgical excision and the tissue was sliced into blocks of approximately 35×20×2 mm^3 to fit a 3D printed mold and scanned at a Bruker 9.4 T BioSpec Avance III scanner (Figure 13B). Diffusion tensor imaging (DTI) was performed with TR=2.5 s, TE=30 ms, resolution=200×200×200 μm^3, and *b*-values of 100, 1000 and 3000 s/mm^2, applied in 6 directions. Measured parameters were MD, FA and in-plane FA (FA_{IP}). The maps were smoothed using a Gaussian kernel with a width of 40 μm to reduce the impact of coregistration errors. After imaging, specimens were sliced into 4–5 μm thick slices, stained with Hematoxylin & Eosin (H&E) and scanned with a light microscope at resolution 0.5×0.5 μm^2. MR and histology images were coregistered by a non-rigid landmark-based approach. These were defined on the MD and FA_{IP} maps and matched with features on the histology slices. In particular, some were placed at the edges of the slices but also in tumor microfeatures, such as tumor microvasculature, which could have been identified both in the histology slices and MR images.

Cell nuclei from histology images were detected by the QuPath (version 0.23) cell detection algorithm (Bankhead et al., 2017) and downsampled to MR resolution, by which a cell density (CD) map was generated.

Histology-resolution image anisotropy was obtained from a structure tensor analysis based on Budde and Frank (2012). This consists of computing a structure tensor **H** (Bigun, 1987;Budde and Frank, 2012),

$$\mathbf{H} = \begin{pmatrix} H_{xx} & H_{xy} \\ H_{xy} & H_{yy} \end{pmatrix}, \tag{9.1.1}$$

where H_{xx}, H_{yy} and H_{xy} are partial spatial image derivatives along x or y directions. These were computed as convolution of the histology image with derivative filter along x or y direction smoothed with a Gaussian filter of size 4.5 μm and standard deviation σ = 0.25 μm. Finally, the obtained structure tensor **H** was smoothed by another Gaussian filter of size 25.5 μm and σ = 15 μm and downsampled to the MR. Image anisotropy was calculated from the eigenvalues λ_1 and λ_2 of the downsampled **H** as

$$\mathrm{IA} = \frac{\lambda_1 - \lambda_2}{\lambda_1 + \lambda_2}, \tag{9.1.2}$$

where $\lambda_1 > \lambda_2$. Finally, the IA maps were smoothed with the same Gaussian kernel as the dMRI maps (σ = 40 μm) for comparability and to reduce the impact of coregistration errors.

We used a similar approach based on Eq. 9.1.1 and Eq. 9.1.2 to compute FA_{IP}. Here, we replaced image derivatives, such as H_{ij}, from structure tensor **H** (Eq. 9.1.1) with the apparent diffusion coefficients D_{ij} selected from the full diffusion tensor **D** (Eq. 5.1.7) by setting $D_{xz} = D_{yz} = D_{zz} = 0$.

The calculated features from histology, IA and CD, were used in a regression analysis to predict measured dMRI maps, MD and FA_{IP}. First, scatter plots of CD vs MD as well as IA vs FA_{IP} were investigated to find out which fitting function best explains the data: by first-, second- and third-degree polynomials. We settled on the second-order polynomial for both modalities and all cases. Second, we randomly selected 80 % of the voxels within each single sample and used them to fit the second-order polynomial and then predict the dMRI maps individually for both modalities and all cases.

We also predicted both MD and FA_{IP} using an artificial neural network (ANN). The network was trained to predict values in an individual voxels using a spatially corresponding 360×360 pixels patch of the histology images (Figure 13B, part 5). After experimentation, we settled on using an EfficientNetV2 network pretrained on the ImageNet dataset (Tan and Le, 2021) and fine-tuned it for the patch-to-value regression task. The training was performed separately on each sample and individually for both modalities. We used horizontal and vertical image flipping for data augmentation and a train-validation-test split of 60/20/20 %.

The two approaches (prediction by calculated features and the ANN) were evaluated using the coefficient of determination (R^2) on the test sets. The residual map (difference between predicted measured map) was also investigated and voxels with large positive or negative residuals were investigated in order to define additional features that may be of relevance (Figure 13C).

A. Zoom-in on different meningioma types

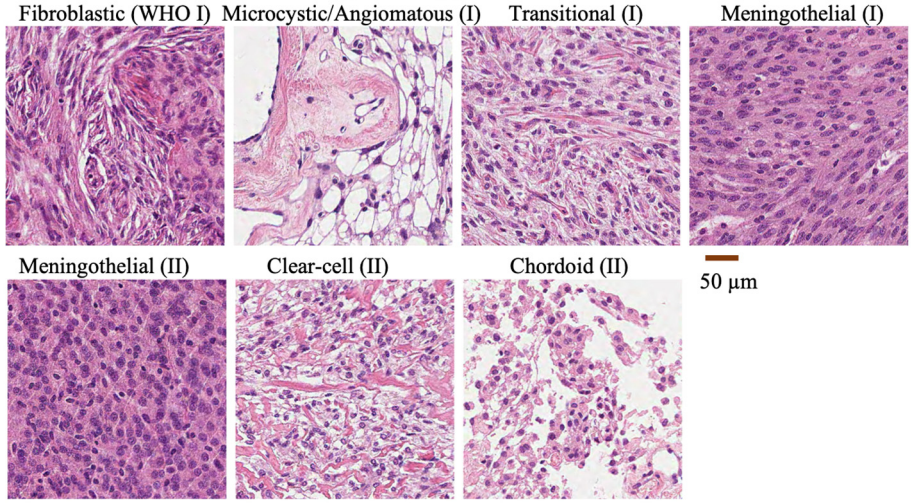

B. The meningioma study design

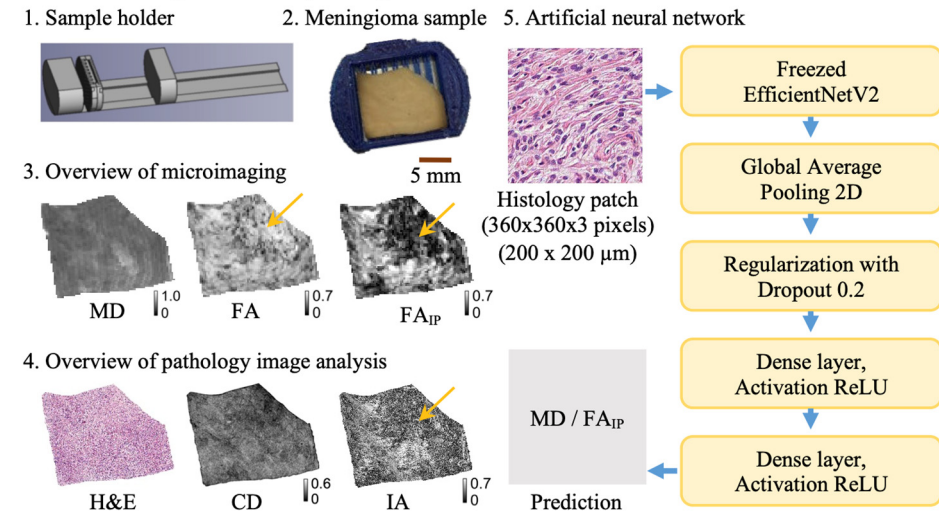

C. Investigation of missing features on residual maps

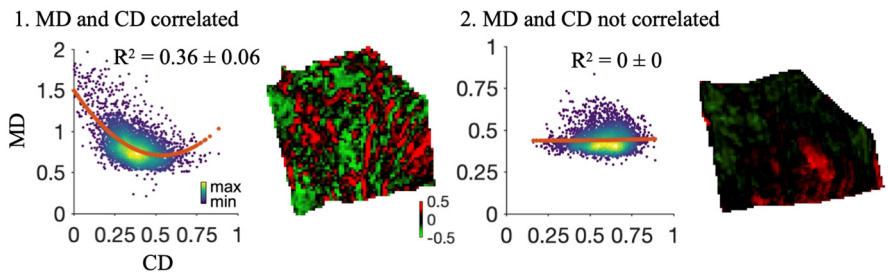

Figure 13. Meningioma tumor heterogeneity and methods overview. Panel A shows that the microstructure is heterogeneous among different meningioma subtypes and even within a single image voxel (Paper II). Panel B shows methods overview of the meningioma study. Part 1 shows a schematics of a 3D-printed sample holder that was used to facilitate voxel-to-voxel coregistration. Panel 2 shows a meningioma sample in the holder. Panel 3 shows obtained dMRI maps: mean diffusivity (MD), fractional anisotropy (FA) and also in-plane fractional anisotropy (FA_{IP}) which disregards in-and-out plane diffusion. For example, in the upper right part of the tumor (yellow arrows) the anisotropy is dominant in the out-of-plane direction and thus FA is high but FA_{IP} low. Panel 4 shows a coregistered histology slice (H&E stained) that was processed to obtain cell density (CD, cell nuclei count density) and image anisotropy (IA from structure tensor analysis). Panel 5 shows an overview of the artificial neural network architecture (ANN). Panel C shows how MD was predicted from CD. We predicted MD based on second-degree polynomial fit in all cases and generated maps that show the residual in individual voxels. Red color shows underestimated voxels where a "free" compartments may need to be added to yield unbiased predictions whereas green color shows overestimated MD where rather a "restriction" should be added. Part 1 shows a sample where MD was relatively well predicted by CD whereas part 2 shows a sample where MD was not well predicted by CD. Figure adapted from Paper II.

9.2. CD and IA as explanations for MD and FA_{IP}?

Across tumors on the whole-sample level, we reproduced linear associations between CD and MD ($R^2 = 0.58$ between CD and MD), as well as between IA and FA_{IP} ($R^2 = 0.82$ between IA and FA_{IP}). However, within tumors on the mesoscopic level (200 μm) the second-order degree polynomial of CD and IA poorly explained the intra-tumor variability of the corresponding dMRI observables. MD had R^2 = 0.06 (0.01 – 0.29) (median (interquartile range)) with R^2 ranging from 0 to 0.43 (Figure 14A) and FA_{IP} had $R^2 = 0.16$ (0.06 – 0.20) and values from 0 to 0.32 (Figure 14B). The intra-tumor variability in MD and FA_{IP} was slightly better explained by the ANN. Across samples, MD had $R^2 = 0.19$ (0.09 - 0.29) with R^2 ranging from 0 to 0.61 (Figure 13A) and FA_{IP} had $R^2 = 0.18$ (0.09 - 0.34) and R^2 ranging from 0 to 0.39) (Figure 13B).

In summary, lower R^2 of predictions on the mesoscopic level compared to the whole-sample indicates that CD and IA are more useful when explaining global rather than local variability. Furthermore, the discrepancy between the R^2 of prediction from ANN and that of CD or IA at the mesoscopic level indicates that features apart from CD and IA may be important for the explanation of the local variability of MD and FA_{IP}. The variability of MD in a substantial number of samples (6 out of 16) was not explained by CD, although it was much better explained by ANN.

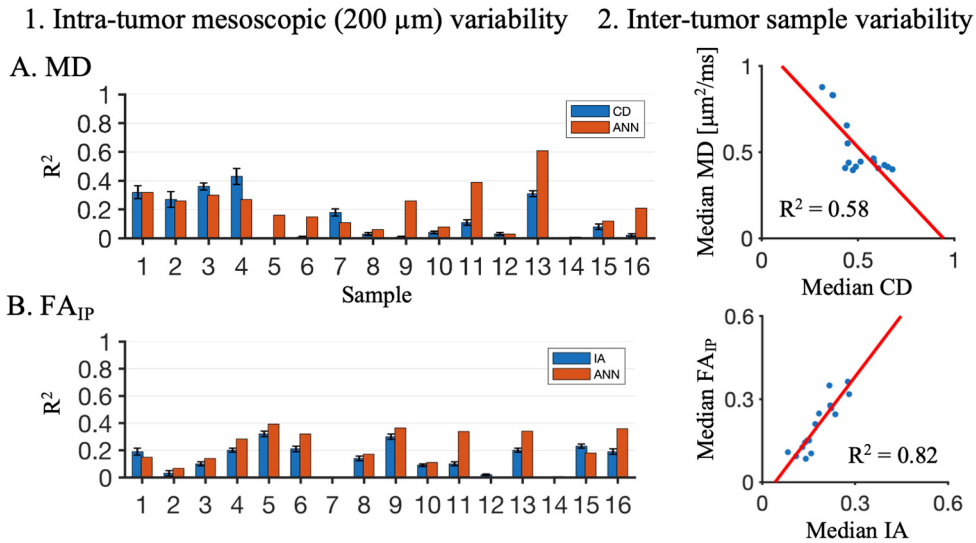

Figure 14. Variability in MD and FA_{IP}. The variability is explained by cell density (CD) and image anisotropy (IA), respectively, as well as artificial neural network (ANN). Panel A shows intra-tumor sample variability (R^2) in MD explained by CD (blue bars corresponds to median, black error bars show interquartile range) and by an artificial neural network (ANN; red bars), respectively. Panel B shows intra-tumor sample variability (R^2) in FA_{IP} explained by IA (blue bars corresponds to median, black error bars show interquartile range) and by artificial neural network (ANN; red bars), respectively. Figure adapted from Paper II.

9.3. Relevant features to MD beyond cell density

We studied what microstructural features correspond to MR voxels where the MD predicted by the second-degree polynomial of CD was underestimated (marked by blue borders), overestimated (purple borders) or well estimated (black borders) (Figure 13C). We separated these into three categories, because it was instructive concerning what impact the features may have on the diffusion. In the case of underestimated MD a "free" compartment may be added to yield unbiased prediction. In the case of overestimated MD a "restriction" should be added, and in the case of well-estimated MD no additional features are needed.

First, both low and high CD can lead to similar MD even though that both voxels have low residuals and MD is overall well explained by CD (R^2 = 0.36). The left image in the Figure 15A shows a voxel with low CD that contains tumor stroma, vessels and microcysts, whereas the right image has high CD and is characterized by a tumor mass, fewer microcysts and vessels. This is illustrative because despite high R^2 there is still significant variability and the discrepancy in this case may be explained by the fact that tumor stroma with few cells may restrict the diffusion more than a tumor mass with more cells. Second, in some cases, cell sizes may

explain why low and high CD are associated with similar MD. Figure 15B shows a case with low CD that contains cells with a rather large cytoplasm volume, whereas the voxel with high CD shows smaller cells with small cytoplasm volume. Both voxels have low residual, and the MD of the whole sample was overall not explained by CD ($R^2 = 0$). This indicates that it is the intracellular volume fraction rather than cell density that is relevant for MD. Third, tissue cohesivity may also be also relevant for explaining of the under- and overestimated MD. The Figure 15C shows tightly-packed tissue with collagen with underestimated MD. The in voxel on the right shows rather loose tissue with few vessels with overestimated MD. Fourth, tumor vasculature was associated with underestimated MD. This is shown in Figure 15D on the left, and for comparison a voxel without residual that contains tumor mass is shown on the right. Therefore, tumor vasculature could provide a "free" additional compartment by which the MD underestimation could be partially corrected. Fifth, tightly packed microcysts were associated with an overestimated MD. This is shown in Figure 15D on the left and on the right is shown a voxel without residual that contains tumor mass. Small and tightly packed microcysts may represent a "restrictive" compartment that may correct the overestimated MD. Finally, psammoma bodies tend to be associated with overestimated MD as shown in Figure 15F on the left. On the right is shown a voxel that contains tumor mass and has low residual.

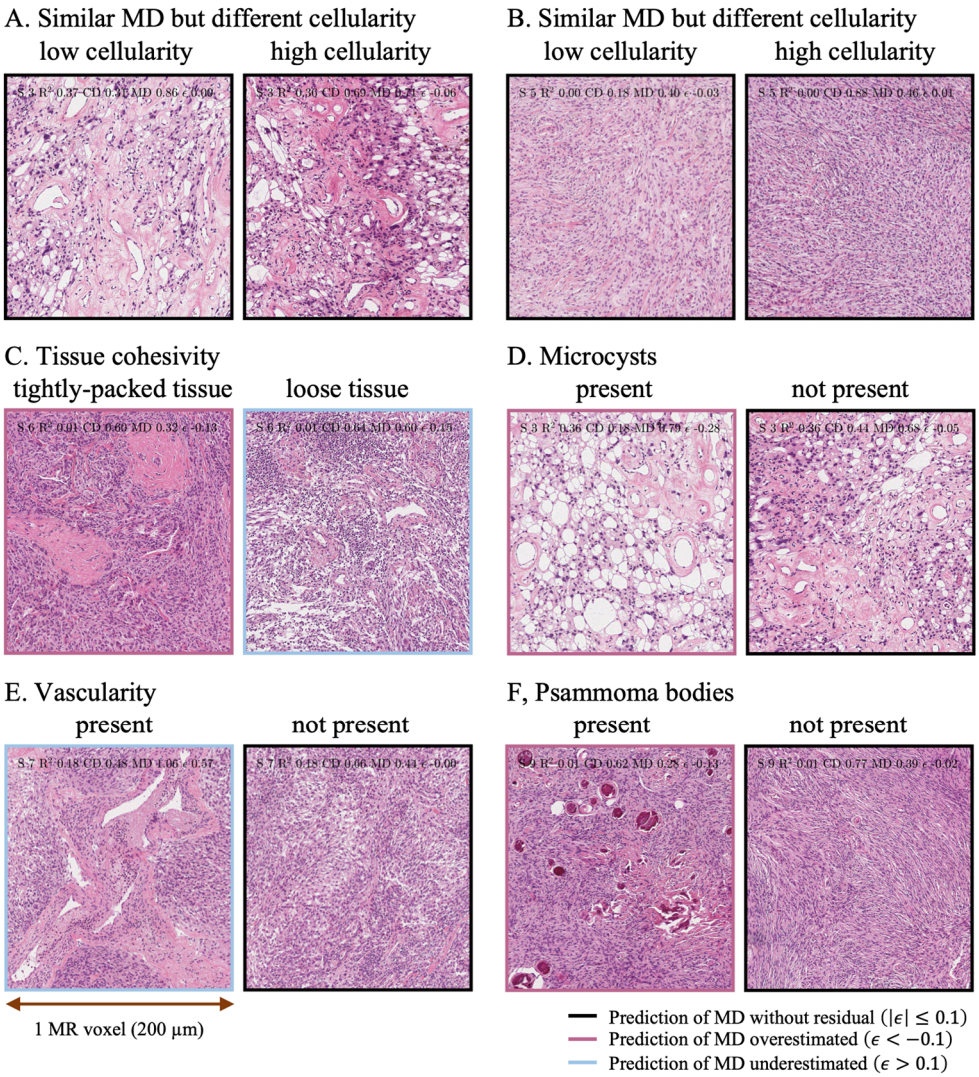

Figure 15. Histological features beyond cell density that may affect MD. Panel A shows a case where both low and high cell density leads to similar MD in a voxel where MD is well predicted (without residual; marked by black borders) and the sample has overall strong association between CD and MD (R^2 = 0.36). The left image shows a voxel with low CD that contains tumor stroma, vessels and microcysts while the one on the right has high CD and is associated rather with denser tumor mass and fewer microcysts. Panel B shows a similar case in another sample but with no association (R^2 = 0.00). The voxel on the left with low CD has larger cell with larger cytoplasm whereas the opposite holds for the voxel with high CD. Panel C shows that MD can be linked to tissue cohesivity. The overestimated voxel (purple border) is associated with tightly-packed tissue with collagen whereas the underestimated one (blue) features loose tissue with few vessels. Panel D shows that overestimated MD can be linked to tightly packed microcysts. The control voxel (without residual) features tumor mass and fewer microcysts. Panel E shows that a voxel with underestimated MD contains tumor vasculature, while the control voxel contains no large vessels but only tumor mass. Finally, panel F shows a voxel with overestimated MD that could also be attributed to psammoma bodies because the control voxel does not feature them. S = sample number, ε = residual (measured MD – predicted MD in a particular voxel). A MR voxel with MD and with low residual is shown with black borders, and overestimated MD with purple and underestimated with blue border. Figure adapted from Paper II.

9.4. FA_{IP} linked to IA offset by tissue orientation dispersion

Image anisotropy is a feature of an image that is not directly linked to the tissue microstructure. This means that it is not evident what type of microstructure is associated with elevated or decreased IA and that is why we investigated voxels with high and low IA without residuals in samples with overall high R^2.

High IA and high FA_{IP} reflected anisotropic tissue with structures oriented along a single direction, whereas low IA and low FA_{IP} reflected tissue that is oriented in multiple directions on the scale of the image voxel, although it can be anisotropic on a scale smaller than the image voxel. In particular, panel A of Figure 16 shows three microstructure examples corresponding to voxels with high IA and high FA_{IP} without residual in a sample with high R^2. The left and middle images show anisotropic tissue that is dominantly oriented along a single direction, whereas the image on the right shows tissue with few orientations. Panel B shows another three microstructure examples corresponding to voxels with low IA and low FA_{IP} without residual in a sample with high R^2. Unlike in the previous panel, the tissue is not oriented along a single direction, even if it is slightly anisotropic. On the voxel-level it appears isotropic due to the high orientation dispersion. Panel C shows cases that may not intuitively be associated with high tissue anisotropy but that regardless gives high IA: the boundary between tumor and vessels (left); transition from tumor tissue to microcysts (middle); or tissue looseness with white transparent areas (right). These cases showed low to intermediate FA, and they illustrate a limitation of the structure tensor analysis.

These considerations may explain why MK_A from QTI was positively associated with firm meningioma consistency while FA was not, as described in the chapter 8.2. This is because FA and MK_A both reflect diffusion anisotropy but on different length-scales. Whereas FA (Eqs. 5.1.11 and 5.2.12) corresponds to the "macroscopic" voxel-level average diffusion anisotropy, MK_A (Eq. 5.2.10) reflects "microscopic" diffusion anisotropy in the microenvironments (Szczepankiewicz et al., 2016). This means that FA is lower than MK_A due to low orientation dispersion.

Low FA may be due to isotropic diffusivity in the microenvironments or due to high microscopic diffusion anisotropy combined with high orientation dispersion (Szczepankiewicz et al., 2016). High FA values are found only due to high microscopic diffusion anisotropy in combination with low orientation dispersion. On the other hand, MK_A is not sensitive to the orientation dispersion and is high when the diffusion anisotropy is high and low when the diffusion anisotropy is low, which means that it has more specific interpretation.

We could hypothesize that meningioma firmness is related to the presence of voxels that have lower diffusion anisotropy and lower orientation dispersion than soft or

variable consistency because $MK_{A\ 10}$ was significantly lower in firm meningiomas, but FA was similar (Figure 12AB) (Paper V). Other studies found that FA preoperatively predicts meningioma consistency (Kashimura et al., 2007), whereas others found it did not (Ortega-Porcayo et al., 2015). As low FA can be both due to high orientation dispersion or low diffusion anisotropy, it is difficult to interpret such findings in terms of microstructure. Future studies using MK_A would be better positioned to do so.

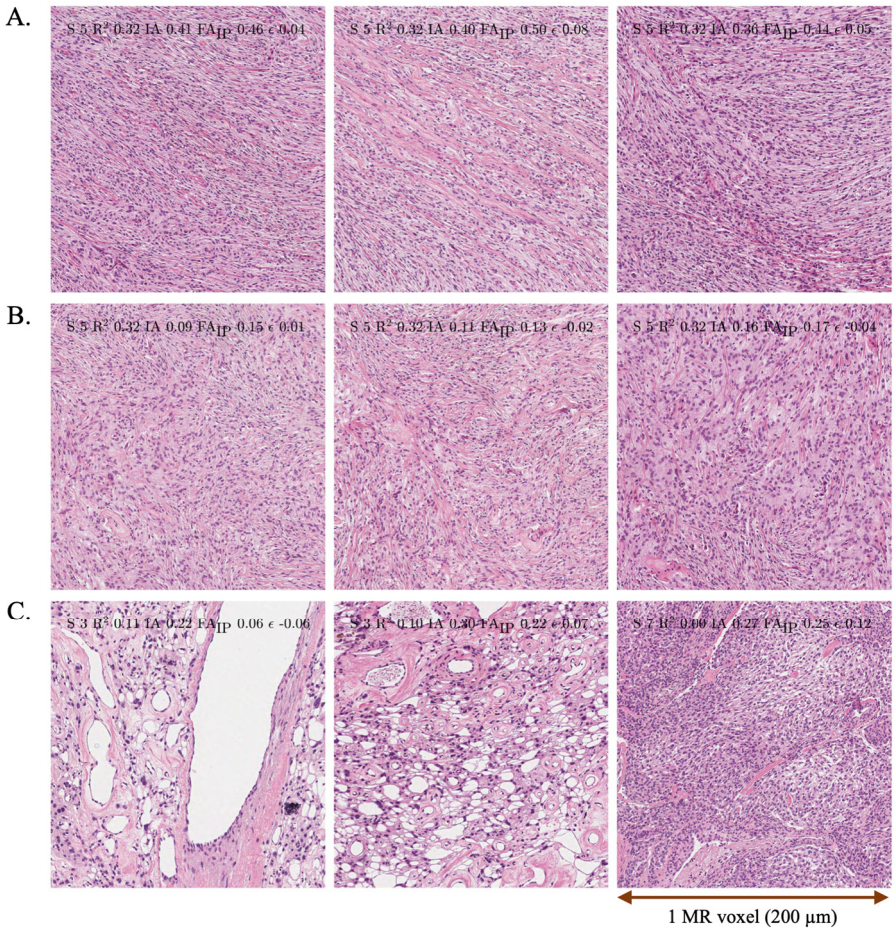

Figure 16. Interpretation of local variations of FA_{IP} and image anisotropy (IA). Panel A illustrates that tissue with elongated structures that are dominantly oriented along a single direction yield high diffusion anisotropy (high IA and high FA_{IP}). Panel B features tissue structures oriented without any single preferential direction, which yield low diffusion anisotropy and thus appears as isotropic tissue (low IA and low FA_{IP}). Panel C shows tissues with boundaries between tumor and vessels (left), transition from tumor tissue to microcysts (middle) or tissue looseness with white transparent areas (right). These yield high IA but have little influence of the diffusion and thus yield low to intermediate FA_{IP} and illustrates a limitation of the technique. Figure adapted from Paper II.

9.5. Conclusions

In Paper II, we reproduced associations between CD and MD ($R^2 = 0.58$) and IA and FA_{IP} ($R^2 = 0.82$) across samples. However, within samples the association between CD and MD was weak or even absent in some samples. The ANN approach performed slightly better, meaning there is information in the histology images capable of explaining additional variation in the dMRI maps. Based on a qualitative analysis, we speculate that features such as tumor vascularization, psammoma bodies, microcysts or tissue cohesivity apart from CD are of importance for the local interpretability of MD.

10. Conclusions

Diffusion MRI is typically interpreted in terms of simple features of the microstructure such as the cell density in the case of MD or the axon diameter in the case of time-dependent diffusion. However, we found that mesoscopic features of the tissue need to be considered when interpreting dMRI.

- In Paper I, we found that fiber undulations contribute to a diffusion time-dependence similar to that of straight-cylinders. Axonal undulations can thus bias diameter estimation strategies if straight cylinders are used to model the intra-axonal diffusion for axons with non-straight trajectories. Diffusion encoding with encoding power at higher frequencies might help resolve effects of undulations and sizes.
- In Paper II, we found that cell density and image anisotropy account for variability in MD and in-plane FA across tumors but not generally within tumors. Features such as tumor vascularization, psammoma bodies, microcysts and cell cohesivity likely all contribute to the dMRI observables.

In our second group of aims we found that advanced diffusion MRI encoding is feasible in a clinical setting and can add value to cancer imaging.

- In Paper III, we investigated the potential utility of diffusion-weighted imaging (DWI) with spherical tensor-valued encoding (STE) in glioma hyperintensities unrelated to white matter. We found that high *b*-value STE-DWI results in a stronger suppression of white matter than conventional LTE-DWI and may therefore be more sensitive and specific for the assessment of glioma tumors and DWI-hyperintensities.
- In Paper IV, we found that evaluation of the iso- and anisotropic kurtoses (MK_I and MK_A) in intracranial tumor patients is feasible in clinically relevant scan times. An imaging protocol with 3-minutes of scan time yielded performance similar to that of the full longer protocol.
- In Paper V, we found that parameters from tensor-valued dMRI may facilitate the prediction of meningioma consistency, grade and type. For example, the lower 10^{th} percentiles of MK and MK_A were associated with firm consistency, higher standard deviation of MK_I was associated with lower grade. Parameters specific to tensor-valued dMRI (MK_A and MK_I) were the only ones that could separate the psammomatous meningiomas.

Acknowledgements

I would like to express gratitude to my main supervisor Markus Nilsson for his support as well as to my co-supervisors Filip Szczepankiewicz and Linda Knutsson. Furthermore, I would like to thank all the co-authors for their contributions.

I would also like to thank to the whole MR physics group in Lund as well as to all current and past colleagues for time during and outside of work: Anina, Annika, Anna, Andrea, Arthur, Axel, Björn, Boel, C-F, Daniel, Danielle, Elisabet, Elise, Emelie, Emil, Evgenios, Faris, Finn, Freddy, Frederik, Geraline, Gregory, Gunther, Hampus, Jaromír, Johan, Jimmy, João, Johan, Johannes, Jonas, Karin, Lara, Laura, Lovisa, Lubomír, Mads, Magda, Martin, Marjolein, Michael, Natalia, Nicola, Niccolo, Olof, Oscar, Patrick, Patrik, Pia, Philip, Renné, Sajad, Samo, Samuel, Teresa, Theo, Till, Titti and all the staff behind the scenes!

A special thanks to friends from Lund: Vendy for the sweat, Jan for towing and being a great PIC, Jannu, Kaidi and the whole group in the Czech and USA. Thanks to Landskrona flygklubb, Krav Maga Lund and the volleyball team.

I would also like to thank my parents for their tireless support. Thank You, dear Anna – without You there would only remain pain and suffering (drama!). Finally, a hat tip to the cat Sheila who meows only in the times of need.

Funding

- Swedish Research Council (2016-03443, 2016-02199-3, 2019-01162, 2020-04549, 2021-04844)
- Swedish Cancer Society (2016-365, 2018-468, 2019-0474)
- Swedish Foundation for Strategic Research (AM13–0090)
- Crafoord Foundation (20160990, 20170825)
- Random Walk Imaging AB (MN15)
- National Institutes of Health (R01MH074794, P41EB015902)
- Regional grant support ALF (2018-1490).

References

Abdollahzadeh, A., Belevich, I., Jokitalo, E., Tohka, J., and Sierra, A. (2019). Automated 3D axonal morphometry of white matter. *Scientific reports* 9**,** 1-16.

Aboitiz, F., Scheibel, A.B., Fisher, R.S., and Zaidel, E. (1992). Fiber composition of the human corpus callosum. *Brain research* 598**,** 143-153.

Afzali, M., Aja-Fernández, S., and Jones, D.K. (2020). Direction-averaged diffusion-weighted MRI signal using different axisymmetric B-tensor encoding schemes. *Magnetic resonance in medicine* 84**,** 1579-1591.

Afzali, M., Mueller, L., Szczepankiewicz, F., Jones, D.K., and Schneider, J.E. (2022). Quantification of tissue microstructure using tensor-valued diffusion encoding: brain and body. *Frontiers of Physics*.

Afzali, M., Nilsson, M., Palombo, M., and Jones, D.K. (2021). SPHERIOUSLY? The challenges of estimating sphere radius non-invasively in the human brain from diffusion MRI. *NeuroImage* 237**,** 118183.

Alexander, D.C., Dyrby, T.B., Nilsson, M., and Zhang, H. (2019). Imaging brain microstructure with diffusion MRI: practicality and applications. *NMR in Biomedicine* 32**,** e3841.

Alexander, D.C., Hubbard, P.L., Hall, M.G., Moore, E.A., Ptito, M., Parker, G.J., and Dyrby, T.B. (2010). Orientationally invariant indices of axon diameter and density from diffusion MRI. *Neuroimage* 52**,** 1374-1389.

Andersen, K.W., Lasič, S., Lundell, H., Nilsson, M., Topgaard, D., Sellebjerg, F., Szczepankiewicz, F., Siebner, H.R., Blinkenberg, M., and Dyrby, T.B. (2020). Disentangling white-matter damage from physiological fiber orientation dispersion in multiple sclerosis. *Brain Communications*.

Assaf, Y., and Basser, P.J. (2005). Composite hindered and restricted model of diffusion (CHARMED) MR imaging of the human brain. *Neuroimage* 27**,** 48-58.

Assaf, Y., Blumenfeld-Katzir, T., Yovel, Y., and Basser, P.J. (2008). AxCaliber: a method for measuring axon diameter distribution from diffusion MRI. *Magnetic resonance in medicine* 59**,** 1347-1354.

Bain, A.C., Shreiber, D.I., and Meaney, D.F. (2003). Modeling of microstructural kinematics during simple elongation of central nervous system tissue. *J. Biomech. Eng.* 125**,** 798-804.

Bankhead, P., Loughrey, M.B., Fernández, J.A., Dombrowski, Y., Mcart, D.G., Dunne, P.D., Mcquaid, S., Gray, R.T., Murray, L.J., and Coleman, H.G. (2017). QuPath: Open source software for digital pathology image analysis. *Scientific reports* 7**,** 1-7.

Barazany, D., Basser, P.J., and Assaf, Y. (2009). In vivo measurement of axon diameter distribution in the corpus callosum of rat brain. *Brain* 132**,** 1210-1220.

Basser, P.J., Mattiello, J., and Lebihan, D. (1994). MR diffusion tensor spectroscopy and imaging. *Biophysical journal* 66**,** 259-267.
Basser, P.J., and Pierpaoli, C. (2011). Microstructural and physiological features of tissues elucidated by quantitative-diffusion-tensor MRI. *Journal of magnetic resonance* 213**,** 560-570.
Beaulieu, C. (2002). The basis of anisotropic water diffusion in the nervous system–a technical review. *NMR in Biomedicine* 15**,** 435-455.
Bigun, J. (1987). "Optimal orientation detection of linear symmetry". Linköping University Electronic Press).
Blackband, S.J., Flint, J.J., Hansen, B., Shepherd, T.M., Lee, C.H., Streit, W.J., and Forder, J.R. (2020). On the Origins of Diffusion MRI Signal Changes in Stroke. *Frontiers in neurology* 11.
Brant, W.E., and Helms, C.A. (2012). Fundamentals of diagnostic radiology.
Brown, R.W., Haacke, E.M., Cheng, Y.-C.N., Thompson, M.R., and Venkatesan, R. (2014). *Magnetic resonance imaging: physical principles and sequence design.* John Wiley & Sons.
Budde, M.D., and Frank, J.A. (2012). Examining brain microstructure using structure tensor analysis of histological sections. *Neuroimage* 63**,** 1-10.
Bulakbasi, N. (2009). Diffusion-tensor imaging in brain tumors. *Imaging in Medicine* 1**,** 155.
Callaghan, P., and Komlosh, M. (2002). Locally anisotropic motion in a macroscopically isotropic system: displacement correlations measured using double pulsed gradient spin-echo NMR. *Magnetic Resonance in Chemistry* 40**,** S15-S19.
Chakwizira, A., Westin, C.-F., Brabec, J., Lasič, S., Knutsson, L., Szczepankiewicz, F., and Nilsson, M. (2021). Probing restricted diffusion and exchange using free gradient waveforms: validation by numerical simulations. *arXiv preprint arXiv:2111.11094*.
Chartrain, A.G., Kurt, M., Yao, A., Feng, R., Nael, K., Mocco, J., Bederson, J.B., Balchandani, P., and Shrivastava, R.K. (2019). Utility of preoperative meningioma consistency measurement with magnetic resonance elastography (MRE): a review. *Neurosurgical review* 42**,** 1-7.
Chen, L., Liu, M., Bao, J., Xia, Y., Zhang, J., Zhang, L., Huang, X., and Wang, J. (2013). The correlation between apparent diffusion coefficient and tumor cellularity in patients: a meta-analysis. *PloS one* 8**,** e79008.
Clark, C.A., Hedehus, M., and Moseley, M.E. (2001). Diffusion time dependence of the apparent diffusion tensor in healthy human brain and white matter disease. *Magnetic Resonance in Medicine: An Official Journal of the International Society for Magnetic Resonance in Medicine* 45**,** 1126-1129.
Clark, D.L., Boutros, N.N., and Mendez, M.F. (2010). *The brain and behavior: an introduction to behavioral neuroanatomy.* Cambridge university press.
Colvin, D.C., Jourquin, J., Xu, J., Does, M.D., Estrada, L., and Gore, J.C. (2011). Effects of intracellular organelles on the apparent diffusion coefficient of water molecules in cultured human embryonic kidney cells. *Magnetic Resonance in Medicine* 65**,** 796-801.

Cory, D.G., Garroway, A.N., and Miller, J.B. (1990). Applications of spin transport as a probe of local geometry. *American Chemical Society, Polymer Preprints, Division of Polymer Chemistry* 31**,** 149-150.

De Almeida Martins, J.P., Tax, C.M., Reymbaut, A., Szczepankiewicz, F., Chamberland, M., Jones, D.K., and Topgaard, D. (2021). Computing and visualising intra-voxel orientation-specific relaxation–diffusion features in the human brain. *Human brain mapping* 42**,** 310-328.

De Almeida Martins, J.P., and Topgaard, D. (2018). Multidimensional correlation of nuclear relaxation rates and diffusion tensors for model-free investigations of heterogeneous anisotropic porous materials. *Scientific reports* 8**,** 1-12.

De Swiet, T.M., and Mitra, P.P. (1996). Possible systematic errors in single-shot measurements of the trace of the diffusion tensor. *Journal of Magnetic Resonance, Series B* 111**,** 15-22.

Delgado, A.F., Fahlström, M., Nilsson, M., Berntsson, S.G., Zetterling, M., Libard, S., Alafuzoff, I., Van Westen, D., Lätt, J., and Smits, A. (2017). Diffusion kurtosis imaging of gliomas grades II and III-a study of perilesional tumor infiltration, tumor grades and subtypes at clinical presentation. *Radiology and oncology* 51**,** 121-129.

Dhital, B., Kellner, E., Kiselev, V.G., and Reisert, M. (2018). The absence of restricted water pool in brain white matter. *Neuroimage* 182**,** 398-406.

Does, M.D., Parsons, E.C., and Gore, J.C. (2003). Oscillating gradient measurements of water diffusion in normal and globally ischemic rat brain. *Magnetic resonance in medicine* 49**,** 206-215.

Edgar, J.M., and Griffiths, I.R. (2009). "White matter structure: a microscopist's view," in *Diffusion Mri*. Elsevier), 74-103.

Egnell, L., Vidić, I., Jerome, N.P., Bofin, A.M., Bathen, T.F., and Goa, P.E. (2020). Stromal Collagen Content in Breast Tumors Correlates With In Vivo Diffusion-Weighted Imaging: A Comparison of Multi b-Value DWI With Histologic Specimen From Benign and Malignant Breast Lesions. *Journal of Magnetic Resonance Imaging* 51**,** 1868-1878.

Einstein, A. (1905). Über die von der molekularkinetischen Theorie der Wärme geforderte Bewegung von in ruhenden Flüssigkeiten suspendierten Teilchen. *Annalen der physik* 322**,** 549-560.

Eriksson, S., Lasič, S., Nilsson, M., Westin, C.-F., and Topgaard, D. (2015). NMR diffusion-encoding with axial symmetry and variable anisotropy: Distinguishing between prolate and oblate microscopic diffusion tensors with unknown orientation distribution. *The Journal of chemical physics* 142**,** 104201.

Eriksson, S., Lasic, S., and Topgaard, D. (2013). Isotropic diffusion weighting in PGSE NMR by magic-angle spinning of the q-vector. *Journal of Magnetic Resonance* 226**,** 13-18.

Essayed, W.I., Zhang, F., Unadkat, P., Cosgrove, G.R., Golby, A.J., and O'donnell, L.J. (2017). White matter tractography for neurosurgical planning: A topography-based review of the current state of the art. *NeuroImage: Clinical* 15**,** 659-672.

Fieremans, E., Burcaw, L.M., Lee, H.-H., Lemberskiy, G., Veraart, J., and Novikov, D.S. (2016). In vivo observation and biophysical interpretation of time-dependent diffusion in human white matter. *Neuroimage* 129**,** 414-427.

Giese, A., Kluwe, L., Laube, B., Meissner, H., Berens, M.E., and Westphal, M. (1996). Migration of human glioma cells on myelin. *Neurosurgery* 38**,** 755-764.

Giovanna, M., and Kaye, A.H. (2007). Integrins: molecular determinants of glioma invasion. *Journal of clinical neuroscience* 14**,** 1041-1048.

Greenberg, H.S., Chandler, W.F., and Sandler, H.M. (1999). *Brain tumors.* Oxford University Press.

Hildebrand, C., Remahl, S., Persson, H., and Bjartmar, C. (1993). Myelinated nerve fibres in the CNS. *Progress in neurobiology* 40**,** 319-384.

Jeffery, G. (1996). PNS features of rodent optic nerve axons. *Journal of Comparative Neurology* 366**,** 370-378.

Jelescu, I.O., Palombo, M., Bagnato, F., and Schilling, K.G. (2020). Challenges for biophysical modeling of microstructure. *Journal of Neuroscience Methods* 344**,** 108861.

Jelescu, I.O., Veraart, J., Fieremans, E., and Novikov, D.S. (2016). Degeneracy in model parameter estimation for multi-compartmental diffusion in neuronal tissue. *NMR in Biomedicine* 29**,** 33-47.

Jensen, J.H., Helpern, J.A., Ramani, A., Lu, H., and Kaczynski, K. (2005). Diffusional kurtosis imaging: The quantification of non-gaussian water diffusion by means of magnetic resonance imaging. *Magnetic resonance in medicine* 53**,** 1432-1440.

Jespersen, S.N., Lundell, H., Sønderby, C.K., and Dyrby, T.B. (2013). Orientationally invariant metrics of apparent compartment eccentricity from double pulsed field gradient diffusion experiments. *NMR in Biomedicine* 26**,** 1647-1662.

Jeurissen, B., Leemans, A., Tournier, J.D., Jones, D.K., and Sijbers, J. (2013). Investigating the prevalence of complex fiber configurations in white matter tissue with diffusion magnetic resonance imaging. *Human brain mapping* 34**,** 2747-2766.

Jian, B., Vemuri, B.C., Özarslan, E., Carney, P.R., and Mareci, T.H. (2007). A novel tensor distribution model for the diffusion-weighted MR signal. *NeuroImage* 37**,** 164-176.

Jolapara, M., Kesavadas, C., Radhakrishnan, V., Thomas, B., Gupta, A., Bodhey, N., Patro, S., Saini, J., George, U., and Sarma, P. (2010). Role of diffusion tensor imaging in differentiating subtypes of meningiomas. *Journal of Neuroradiology* 37**,** 277-283.

Jonas, J.B., Müller-Bergh, J., Schlötzer-Schrehardt, U., and Naumann, G. (1990). Histomorphometry of the human optic nerve. *Investigative ophthalmology & visual science* 31**,** 736-744.

Jones, D.K., and Basser, P.J. (2004). “Squashing peanuts and smashing pumpkins”: how noise distorts diffusion-weighted MR data. *Magnetic Resonance in Medicine* 52**,** 979-993.

Jones, D.K., and Cercignani, M. (2010). Twenty-five pitfalls in the analysis of diffusion MRI data. *NMR in Biomedicine* 23**,** 803-820.

Jones, D.K., Knösche, T.R., and Turner, R. (2013). White matter integrity, fiber count, and other fallacies: the do's and don'ts of diffusion MRI. *Neuroimage* 73**,** 239-254.
Jütten, K., Mainz, V., Gauggel, S., Patel, H.J., Binkofski, F., Wiesmann, M., Clusmann, H., and Na, C.-H. (2019). Diffusion tensor imaging reveals microstructural heterogeneity of normal-appearing white matter and related cognitive dysfunction in glioma patients. *Frontiers in oncology* 9**,** 536.
Kamble, A.N., Agrawal, N.K., Koundal, S., Bhargava, S., Kamble, A.N., Joyner, D.A., Kalelioglu, T., Patel, S.H., and Jain, R. (2022). Imaging-based stratification of adult gliomas prognosticates survival and correlates with the 2021 WHO classification. *Neuroradiology***,** 1-14.
Kang, Y., Choi, S.H., Kim, Y.-J., Kim, K.G., Sohn, C.-H., Kim, J.-H., Yun, T.J., and Chang, K.-H. (2011). Gliomas: histogram analysis of apparent diffusion coefficient maps with standard-or high-b-value diffusion-weighted MR imaging—correlation with tumor grade. *Radiology* 261**,** 882-890.
Kashimura, H., Inoue, T., Ogasawara, K., Arai, H., Otawara, Y., Kanbara, Y., and Ogawa, A. (2007). Prediction of meningioma consistency using fractional anisotropy value measured by magnetic resonance imaging. *Journal of neurosurgery* 107**,** 784-787.
Kingsley, P.B. (2006). Introduction to diffusion tensor imaging mathematics: Part I. Tensors, rotations, and eigenvectors. *Concepts in Magnetic Resonance Part A* 28**,** 101-122.
Kiselev, V.G. (2010). The cumulant expansion: an overarching mathematical framework for understanding diffusion NMR. *Diffusion MRI***,** 152-168.
Kiselev, V.G., and Il'yasov, K.A. (2007). Is the "biexponential diffusion" biexponential? *Magnetic Resonance in Medicine* 57**,** 464-469.
Kolakshyapati, M., Adhikari, R.B., Karlowee, V., Takayasu, T., Nosaka, R., Amatya, V.J., Takeshima, Y., Akiyama, Y., Sugiyama, K., and Kurisu, K. (2017). Nonenhancing peritumoral hyperintense lesion on diffusion-weighted imaging in glioblastoma: a novel diagnostic and specific prognostic indicator. *Journal of neurosurgery* 128**,** 667-678.
Kumar, V., Abbas, A.K., and Aster, J.C. (2017). *Robbins basic pathology e-book.* Elsevier Health Sciences.
Lampinen, B., Szczepankiewicz, F., Mårtensson, J., Van Westen, D., Hansson, O., Westin, C.F., and Nilsson, M. (2020a). Towards unconstrained compartment modeling in white matter using diffusion-relaxation MRI with tensor-valued diffusion encoding. *Magnetic resonance in medicine* 84**,** 1605-1623.
Lampinen, B., Szczepankiewicz, F., Mårtensson, J., Van Westen, D., Sundgren, P.C., and Nilsson, M. (2017). Neurite density imaging versus imaging of microscopic anisotropy in diffusion MRI: a model comparison using spherical tensor encoding. *Neuroimage* 147**,** 517-531.
Lampinen, B., Szczepankiewicz, F., Novén, M., Van Westen, D., Hansson, O., Englund, E., Mårtensson, J., Westin, C.F., and Nilsson, M. (2019). Searching for the neurite density with diffusion MRI: challenges for biophysical modeling. *Human brain mapping* 40**,** 2529-2545.

Lampinen, B., Zampeli, A., Björkman-Burtscher, I.M., Szczepankiewicz, F., Källén, K., Compagno Strandberg, M., and Nilsson, M. (2020b). Tensor-valued diffusion MRI differentiates cortex and white matter in malformations of cortical development associated with epilepsy. *Epilepsia* 61**,** 1701-1713.

Lasič, S., Åslund, I., and Topgaard, D. (2009). Spectral characterization of diffusion with chemical shift resolution: highly concentrated water-in-oil emulsion. *Journal of Magnetic Resonance* 199**,** 166-172.

Lasič, S., Nilsson, M., Lätt, J., Ståhlberg, F., and Topgaard, D. (2011). Apparent exchange rate mapping with diffusion MRI. *Magnetic resonance in medicine* 66**,** 356-365.

Lasič, S., Szczepankiewicz, F., Dall'armellina, E., Das, A., Kelly, C., Plein, S., Schneider, J.E., Nilsson, M., and Teh, I. (2020). Motion-compensated b-tensor encoding for in vivo cardiac diffusion-weighted imaging. *NMR in Biomedicine* 33**,** e4213.

Lasič, S., Szczepankiewicz, F., Eriksson, S., Nilsson, M., and Topgaard, D. (2014). Microanisotropy imaging: quantification of microscopic diffusion anisotropy and orientational order parameter by diffusion MRI with magic-angle spinning of the q-vector. *Frontiers in Physics* 2**,** 11.

Lasič, S., Yuldasheva, N., Szczepankiewicz, F., Nilsson, M., Budde, M., Dall'armellina, E., Schneider, J.E., Teh, I., and Lundell, H. (2022). Stay on the beat with tensor-valued encoding: time-dependent diffusion and cell size estimation in ex vivo heart. *Frontiers in Physics***,** 167.

Latour, L.L., Svoboda, K., Mitra, P.P., and Sotak, C.H. (1994). Time-dependent diffusion of water in a biological model system. *Proceedings of the National Academy of Sciences* 91**,** 1229-1233.

Laviolette, P.S., Mickevicius, N.J., Cochran, E.J., Rand, S.D., Connelly, J., Bovi, J.A., Malkin, M.G., Mueller, W.M., and Schmainda, K.M. (2014). Precise ex vivo histological validation of heightened cellularity and diffusion-restricted necrosis in regions of dark apparent diffusion coefficient in 7 cases of high-grade glioma. *Neuro-oncology* 16**,** 1599-1606.

Lawrenz, M., and Finsterbusch, J. (2013). Double-wave-vector diffusion-weighted imaging reveals microscopic diffusion anisotropy in the living human brain. *Magnetic resonance in medicine* 69**,** 1072-1082.

Le Bihan, D. (2003). Looking into the functional architecture of the brain with diffusion MRI. *Nature reviews neuroscience* 4**,** 469-480.

Lee, H.-H., Jespersen, S.N., Fieremans, E., and Novikov, D.S. (2020a). The impact of realistic axonal shape on axon diameter estimation using diffusion MRI. *Neuroimage* 223**,** 117228.

Lee, H.-H., Papaioannou, A., Kim, S.-L., Novikov, D.S., and Fieremans, E. (2020b). A time-dependent diffusion MRI signature of axon caliber variations and beading. *Communications biology* 3**,** 1-13.

Lee, H.-H., Papaioannou, A., Novikov, D.S., and Fieremans, E. (2020c). In vivo observation and biophysical interpretation of time-dependent diffusion in human cortical gray matter. *Neuroimage* 222**,** 117054.

Lee, H.-H., Yaros, K., Veraart, J., Pathan, J.L., Liang, F.-X., Kim, S.G., Novikov, D.S., and Fieremans, E. (2019). Along-axon diameter variation and axonal orientation dispersion revealed with 3D electron microscopy: implications for quantifying

brain white matter microstructure with histology and diffusion MRI. *Brain Structure and Function* 224**,** 1469-1488.
Li, S., Zheng, Y., Sun, W., Lasič, S., Szczepankiewicz, F., Wei, Q., Han, S., Zhang, S., Zhong, X., and Wang, L. (2021). Glioma grading, molecular feature classification, and microstructural characterization using MR diffusional variance decomposition (DIVIDE) imaging. *European Radiology* 31**,** 8197-8207.
Liu, N., Song, S.-Y., Jiang, J.-B., Wang, T.-J., and Yan, C.-X. (2020). The prognostic role of Ki-67/MIB-1 in meningioma: A systematic review with meta-analysis. *Medicine* 99.
Lontis, E.R., Nielsen, K., and Struijk, J.J. (2009). In vitro magnetic stimulation of pig phrenic nerve with transverse and longitudinal induced electric fields: analysis of the stimulation site. *IEEE Transactions on Biomedical Engineering* 56**,** 500-512.
Louis, D.N., Perry, A., Reifenberger, G., Von Deimling, A., Figarella-Branger, D., Cavenee, W.K., Ohgaki, H., Wiestler, O.D., Kleihues, P., and Ellison, D.W. (2016). The 2016 World Health Organization classification of tumors of the central nervous system: a summary. *Acta neuropathologica* 131**,** 803-820.
Louis, D.N., Perry, A., Wesseling, P., Brat, D.J., Cree, I.A., Figarella-Branger, D., Hawkins, C., Ng, H., Pfister, S.M., and Reifenberger, G. (2021). The 2021 WHO classification of tumors of the central nervous system: a summary. *Neuro-oncology* 23**,** 1231-1251.
Lundell, H., Nilsson, M., Dyrby, T., Parker, G., Cristinacce, P.H., Zhou, F.-L., Topgaard, D., and Lasič, S. (2019). Multidimensional diffusion MRI with spectrally modulated gradients reveals unprecedented microstructural detail. *Scientific reports* 9**,** 1-12.
Maggio, I., Franceschi, E., Tosoni, A., Nunno, V.D., Gatto, L., Lodi, R., and Brandes, A.A. (2021). Meningioma: not always a benign tumor. A review of advances in the treatment of meningiomas. *CNS oncology* 10**,** CNS72.
Mattiello, J., Basser, P.J., and Lebihan, D. (1994). Analytical expressions for the b matrix in NMR diffusion imaging and spectroscopy. *Journal of magnetic resonance, Series A* 108**,** 131-141.
Mescher, A. (2021). *Junqueira's Basic Histology, 16th edition, 2021.*
Mills, R. (1973). Self-diffusion in normal and heavy water in the range 1-45. deg. *The Journal of Physical Chemistry* 77**,** 685-688.
Mitra, P.P., Sen, P.N., and Schwartz, L.M. (1993). Short-time behavior of the diffusion coefficient as a geometrical probe of porous media. *Physical Review B* 47**,** 8565.
Mori, S., Crain, B.J., Chacko, V.P., and Van Zijl, P.C. (1999). Three-dimensional tracking of axonal projections in the brain by magnetic resonance imaging. *Annals of Neurology: Official Journal of the American Neurological Association and the Child Neurology Society* 45**,** 265-269.
Mori, S., and Van Zijl, P.C. (1995). Diffusion weighting by the trace of the diffusion tensor within a single scan. *Magnetic resonance in medicine* 33**,** 41-52.
Moseley, M.E., Cohen, Y., Mintorovitch, J., Chileuitt, L., Shimizu, H., Kucharczyk, J., Wendland, M., and Weinstein, P. (1990). Early detection of regional cerebral ischemia in cats: comparison of diffusion-and T2-weighted MRI and spectroscopy. *Magnetic resonance in medicine* 14**,** 330-346.

Nilsson, M., Englund, E., Szczepankiewicz, F., Van Westen, D., and Sundgren, P.C. (2018). Imaging brain tumour microstructure. *Neuroimage* 182**,** 232-250.

Nilsson, M., Lätt, J., Ståhlberg, F., Westen, D., and Hagslätt, H. (2012). The importance of axonal undulation in diffusion MR measurements: a Monte Carlo simulation study. *NMR in Biomedicine* 25**,** 795-805.

Ning, L., Szczepankiewicz, F., Nilsson, M., Rathi, Y., and Westin, C.-F. (2021). Probing tissue microstructure by diffusion skewness tensor imaging. *Scientific Reports* 11**,** 1-10.

Novikov, D.S., Fieremans, E., Jespersen, S.N., and Kiselev, V.G. (2019). Quantifying brain microstructure with diffusion MRI: Theory and parameter estimation. *NMR in Biomedicine* 32**,** e3998.

Novikov, D.S., Jensen, J.H., Helpern, J.A., and Fieremans, E. (2014). Revealing mesoscopic structural universality with diffusion. *Proceedings of the National Academy of Sciences* 111**,** 5088-5093.

Novikov, D.S., Kiselev, V.G., and Jespersen, S.N. (2018). On modeling. *Magnetic resonance in medicine* 79**,** 3172-3193.

Ortega-Porcayo, L.A., Ballesteros-Zebadúa, P., Marrufo-Meléndez, O.R., Ramírez-Andrade, J.J., Barges-Coll, J., Tecante, A., Ramírez-Gilly, M., and Gómez-Amador, J.L. (2015). Prediction of mechanical properties and subjective consistency of meningiomas using T1-T2 assessment versus fractional anisotropy. *World neurosurgery* 84**,** 1691-1698.

Özarslan, E., and Basser, P.J. (2008). Microscopic anisotropy revealed by NMR double pulsed field gradient experiments with arbitrary timing parameters. *The Journal of chemical physics* 128**,** 04B615.

Palombo, M., Ligneul, C., Hernandez-Garzon, E., and Valette, J. (2018). Can we detect the effect of spines and leaflets on the diffusion of brain intracellular metabolites? *Neuroimage* 182**,** 283-293.

Patterson, D.M., Padhani, A.R., and Collins, D.J. (2008). Technology insight: water diffusion MRI—a potential new biomarker of response to cancer therapy. *Nature clinical practice Oncology* 5**,** 220-233.

Price, S.J., Pena, A., Burnet, N.G., Jena, R., Green, H.A., Carpenter, T.A., Pickard, J.D., and Gillard, J.H. (2004). Tissue signature characterisation of diffusion tensor abnormalities in cerebral gliomas. *European radiology* 14**,** 1909-1917.

Reymbaut, A., Caron, A.V., Gilbert, G., Szczepankiewicz, F., Nilsson, M., Warfield, S.K., Descoteaux, M., and Scherrer, B. (2021). Magic DIAMOND: Multi-fascicle diffusion compartment imaging with tensor distribution modeling and tensor-valued diffusion encoding. *Medical Image Analysis* 70**,** 101988.

Ricard, D., Idbaih, A., Ducray, F., Lahutte, M., Hoang-Xuan, K., and Delattre, J.-Y. (2012). Primary brain tumours in adults. *The Lancet* 379**,** 1984-1996.

Ritchie, J.M. (1982). On the relation between fibre diameter and conduction velocity in myelinated nerve fibres. *Proc. R. Soc. Lond. B* 217**,** 29-35.

Romani, R., Tang, W.-J., Mao, Y., Wang, D.-J., Tang, H.-L., Zhu, F.-P., Che, X.-M., Gong, Y., Zheng, K., and Zhong, P. (2014). Diffusion tensor magnetic resonance imaging for predicting the consistency of intracranial meningiomas. *Acta neurochirurgica* 156**,** 1837-1845.

Romano, A., D'andrea, G., Minniti, G., Mastronardi, L., Ferrante, L., Fantozzi, L., and Bozzao, A. (2009). Pre-surgical planning and MR-tractography utility in brain tumour resection. *European radiology* 19**,** 2798-2808.

Schilling, K.G., Janve, V., Gao, Y., Stepniewska, I., Landman, B.A., and Anderson, A.W. (2018). Histological validation of diffusion MRI fiber orientation distributions and dispersion. *Neuroimage* 165**,** 200-221.

Sen, P.N., and Basser, P.J. (2005). A model for diffusion in white matter in the brain. *Biophysical journal* 89**,** 2927-2938.

Seo, H.S., Chang, K.-H., Na, D., Kwon, B., and Lee, D. (2008). High b-value diffusion (b= 3000 s/mm2) MR imaging in cerebral gliomas at 3T: visual and quantitative comparisons with b= 1000 s/mm2. *American Journal of Neuroradiology* 29**,** 458-463.

Shemesh, N., Jespersen, S.N., Alexander, D.C., Cohen, Y., Drobnjak, I., Dyrby, T.B., Finsterbusch, J., Koch, M.A., Kuder, T., and Laun, F. (2016). Conventions and nomenclature for double diffusion encoding NMR and MRI. *Magnetic resonance in medicine* 75**,** 82-87.

Shiroishi, M.S., Cen, S.Y., Tamrazi, B., D'amore, F., Lerner, A., King, K.S., Kim, P.E., Law, M., Hwang, D.H., and Boyko, O.B. (2016). Predicting meningioma consistency on preoperative neuroimaging studies. *Neurosurgery Clinics* 27**,** 145-154.

Sjölund, J., Szczepankiewicz, F., Nilsson, M., Topgaard, D., Westin, C.-F., and Knutsson, H. (2015). Constrained optimization of gradient waveforms for generalized diffusion encoding. *Journal of magnetic resonance* 261**,** 157-168.

Slator, P.J., Palombo, M., Miller, K.L., Westin, C.F., Laun, F., Kim, D., Haldar, J.P., Benjamini, D., Lemberskiy, G., and De Almeida Martins, J.P. (2021). Combined diffusion-relaxometry microstructure imaging: Current status and future prospects. *Magnetic Resonance in Medicine* 86**,** 2987-3011.

Squillaci, E., Manenti, G., Cova, M., Di Roma, M., Miano, R., Palmieri, G., and Simonetti, G. (2004). Correlation of diffusion-weighted MR imaging with cellularity of renal tumours. *Anticancer research* 24**,** 4175-4180.

Stanisz, G.J., Wright, G.A., Henkelman, R.M., and Szafer, A. (1997). An analytical model of restricted diffusion in bovine optic nerve. *Magnetic Resonance in Medicine* 37**,** 103-111.

Stassart, R.M., Möbius, W., Nave, K.-A., and Edgar, J.M. (2018). The axon-myelin unit in development and degenerative disease. *Frontiers in neuroscience***,** 467.

Stejskal, E.O., and Tanner, J.E. (1965). Spin diffusion measurements: spin echoes in the presence of a time-dependent field gradient. *The journal of chemical physics* 42**,** 288-292.

Stepišnik, J. (1993). Time-dependent self-diffusion by NMR spin-echo. *Physica B: Condensed Matter* 183**,** 343-350.

Sung, H., Ferlay, J., Siegel, R.L., Laversanne, M., Soerjomataram, I., Jemal, A., and Bray, F. (2021). Global cancer statistics 2020: GLOBOCAN estimates of incidence and mortality worldwide for 36 cancers in 185 countries. *CA: a cancer journal for clinicians* 71**,** 209-249.

Szafer, A., Zhong, J., and Gore, J.C. (1995). Theoretical model for water diffusion in tissues. *Magnetic resonance in medicine* 33**,** 697-712.

Szczepankiewicz, F., Juvekar, P., Brabec, J., Sundgren, P.C., Nilsson, M., Golby, A., and Westin, C.-F. (2020). Investigation of tumor grade and gadolinium enhancement by tensor-valued diffusion encoding and QTI analysis: an exploratory study of gliomas. *ISMRM Annual Meeting*.

Szczepankiewicz, F., Lasič, S., Van Westen, D., Sundgren, P.C., Englund, E., Westin, C.-F., Ståhlberg, F., Lätt, J., Topgaard, D., and Nilsson, M. (2015). Quantification of microscopic diffusion anisotropy disentangles effects of orientation dispersion from microstructure: applications in healthy volunteers and in brain tumors. *NeuroImage* 104**,** 241-252.

Szczepankiewicz, F., and Sjölund, J. (2021). Cross-term-compensated gradient waveform design for tensor-valued diffusion MRI. *Journal of Magnetic Resonance* 328**,** 106991.

Szczepankiewicz, F., Sjölund, J., Dall'armellina, E., Plein, S., Schneider, J.E., Teh, I., and Westin, C.F. (2021a). Motion-compensated gradient waveforms for tensor-valued diffusion encoding by constrained numerical optimization. *Magnetic resonance in medicine* 85**,** 2117-2126.

Szczepankiewicz, F., Sjölund, J., Ståhlberg, F., Lätt, J., and Nilsson, M. (2019a). Tensor-valued diffusion encoding for diffusional variance decomposition (DIVIDE): Technical feasibility in clinical MRI systems. *PloS one* 14**,** e0214238.

Szczepankiewicz, F., Van Westen, D., Englund, E., Westin, C.-F., Ståhlberg, F., Lätt, J., Sundgren, P.C., and Nilsson, M. (2016). The link between diffusion MRI and tumor heterogeneity: Mapping cell eccentricity and density by diffusional variance decomposition (DIVIDE). *Neuroimage* 142**,** 522-532.

Szczepankiewicz, F., Westin, C.-F., and Nilsson, M. (2021b). Gradient waveform design for tensor-valued encoding in diffusion MRI. *Journal of Neuroscience Methods***,** 109007.

Szczepankiewicz, F., Westin, C.F., and Nilsson, M. (2019b). Maxwell-compensated design of asymmetric gradient waveforms for tensor-valued diffusion encoding. *Magnetic resonance in medicine* 82**,** 1424-1437.

Takagi, T., Nakamura, M., Yamada, M., Hikishima, K., Momoshima, S., Fujiyoshi, K., Shibata, S., Okano, H.J., Toyama, Y., and Okano, H. (2009). Visualization of peripheral nerve degeneration and regeneration: monitoring with diffusion tensor tractography. *Neuroimage* 44**,** 884-892.

Tan, M., and Le, Q. (2021). "Efficientnetv2: Smaller models and faster training", in: *International Conference on Machine Learning*: PMLR), 10096-10106.

Tax, C.M., Szczepankiewicz, F., Nilsson, M., and Jones, D.K. (2020). The dot-compartment revealed? Diffusion MRI with ultra-strong gradients and spherical tensor encoding in the living human brain. *NeuroImage* 210**,** 116534.

Van Cauter, S., Veraart, J., Sijbers, J., Peeters, R.R., Himmelreich, U., De Keyzer, F., Van Gool, S.W., Van Calenbergh, F., De Vleeschouwer, S., and Van Hecke, W. (2012). Gliomas: diffusion kurtosis MR imaging in grading. *Radiology* 263**,** 492-501.

Vandendries, C., Ducreux, D., Lacroix, C., Ducot, B., and Saliou, G. (2014). Statistical analysis of multi-b factor diffusion weighted images can help distinguish between vasogenic and tumor-infiltrated edema. *Journal of Magnetic Resonance Imaging* 40**,** 622-629.

Vis, G., Nilsson, M., Westin, C.-F., and Szczepankiewicz, F. (2021). Accuracy and precision in super-resolution MRI: Enabling spherical tensor diffusion encoding at ultra-high b-values and high resolution. *NeuroImage* 245**,** 118673.

Westin, C.-F., Knutsson, H., Pasternak, O., Szczepankiewicz, F., Özarslan, E., Van Westen, D., Mattisson, C., Bogren, M., O'donnell, L.J., and Kubicki, M. (2016). Q-space trajectory imaging for multidimensional diffusion MRI of the human brain. *Neuroimage* 135**,** 345-362.

White, M.L., Zhang, Y., Yu, F., Shonka, N., Aizenberg, M.R., Adapa, P., and Kazmi, S.a.J. (2019). Post-operative perfusion and diffusion MR imaging and tumor progression in high-grade gliomas. *PloS one* 14.

Wiemels, J., Wrensch, M., and Claus, E.B. (2010). Epidemiology and etiology of meningioma. *Journal of neuro-oncology* 99**,** 307-314.

Wong, E.C., Cox, R.W., and Song, A.W. (1995). Optimized isotropic diffusion weighting. *Magnetic resonance in medicine* 34**,** 139-143.

Xiaoai, K., Qing, Z., Lei, H., and Junlin, Z. (2020). Differentiating microcystic meningioma from atypical meningioma using diffusion-weighted imaging. *Neuroradiology* 62**,** 601-607.

Xu, J., Does, M.D., and Gore, J.C. (2009). Sensitivity of MR diffusion measurements to variations in intracellular structure: effects of nuclear size. *Magnetic Resonance in Medicine: An Official Journal of the International Society for Magnetic Resonance in Medicine* 61**,** 828-833.

Yablonskiy, D.A., and Sukstanskii, A.L. (2010). Theoretical models of the diffusion weighted MR signal. *NMR in Biomedicine* 23**,** 661-681.

Yao, A., Pain, M., Balchandani, P., and Shrivastava, R.K. (2018). Can MRI predict meningioma consistency?: a correlation with tumor pathology and systematic review. *Neurosurgical review* 41**,** 745-753.

Yen, P.S., Teo, B.T., Chiu, C.H., Chen, S.C., Chiu, T.L., and Su, C.F. (2009). White matter tract involvement in brain tumors: a diffusion tensor imaging analysis. *Surgical Neurology* 72**,** 464-469.

Yoshikawa, M.I., Ohsumi, S., Sugata, S., Kataoka, M., Takashima, S., Mochizuki, T., Ikura, H., and Imai, Y. (2008). Relation between cancer cellularity and apparent diffusion coefficient values using diffusion-weighted magnetic resonance imaging in breast cancer. *Radiation medicine* 26**,** 222-226.

Zeng, Q., Ling, C., Shi, F., Dong, F., Jiang, B., and Zhang, J. (2018). Glioma infiltration sign on high b-value diffusion-weighted imaging in gliomas and its prognostic value. *Journal of Magnetic Resonance Imaging* 48**,** 643-651.

Applications of diffusion MRI

In this thesis, we address two shortcomings of diffusion MRI (dMRI).
First, we investigated which microstructural features are of relevance to dMRI. We found that the effects of non-straight propagation of axons are indistinguishable from those originating from the axon diameter for typical measurements with a clinical scanner (panel A). Furthermore, we found that, quantitively, the interpretation of local variability of mean diffusivity and fractional anisotropy by cell density and tissue anisotropy is valid in some but not all tumors (B). Second, we studied what contrasts tensor-valued dMRI can add to the imaging routine of patients with intracranial tumors. We found that it can be applied in a short scan time, enhances the conspicuity of glioma hyperintensities compared to white matter (C) and preoperatively may help to classify meningiomas.

Jan Brabec received M.D. degree and Master in Science degree in Physics.

A

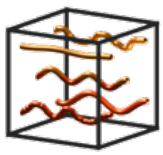

B

C

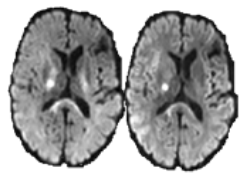

Printed by Media-Tryck, Lund 2022 NORDIC SWAN ECOLABEL 3041 0903

LUND UNIVERSITY

FACULTY OF SCIENCE

Department of Medical Radiation Physics
Faculty of Science
Lund University

978-91-8039-343-0 (electronic)
978-91-8039-344-7 (print)
ISSN 1652-8220